IEEE Access
Multidisciplinary | Rapid Review | Open Access Journal

Received 29 June 2022, accepted 22 July 2022, date of publication 26 July 2022, date of current version 10 August 2022.

Digital Object Identifier 10.1109/ACCESS.2022.3194055

RESEARCH ARTICLE

Design and Implementation of LCL Filter-Based Electric Machine Emulator With Disturbance Compensation

QINGLE SUN, ZHIFU WANG, ZESHANG WANG, AND WENMEI HAO
National Engineering Research Center of Electric Vehicles, School of Mechanical Engineering, Beijing Institute of Technology, Beijing 100081, China
Corresponding author: Zhifu Wang (wangzhifu@bit.edu.cn)

This work was supported in part by the National Natural Science Foundation of China under Grant 51775042.

ABSTRACT The electric machine emulator (EME), using digital simulation and power electronics to emulate the characteristics of actual machines, can greatly accelerate the testing of electric drives. However, most existing EMEs are based on typical L filter and linear controller, which causes control conflicts and bandwidth limitation. To address this issue, this paper presents an EME based on LCL filter with passive damping for a three-phase permanent magnet synchronous motor. To improve the dynamic emulating accuracy, a dual closed-loop deadbeat predictive current control algorithm is proposed, which is computationally efficient and easy to implement. The system stability is analyzed in the discrete domain, and the parameter constraints of the filter are obtained. Then, two unknown input observers are designed to compensate for the disturbance currents and voltages caused by modeling errors. Moreover, instead of the empirical method, a theoretical one considering the harmonic suppression, bandwidth, stability and resonance is presented for filter design. Finally, the performance of the proposed EME is validated through simulation and experimental results under various conditions such as machine start-up, torque step change, and speed reversal.

INDEX TERMS Electric machine emulator (EME), LCL filter, dual closed-loop deadbeat predictive current control, unknown input observer.

NOMENCLATURE

$\omega_{\max}$	Maximum electrical angular frequency.
ω_e	Electrical angular frequency.
ω_{pwm}	Switching frequency of the drive inverter.
C	Filter capacitance.
i_{ed}, i_{eq}	dq-axis currents of the emulating converter.
i_{ld}, i_{lq}	dq-axis disturbance currents.
i_{md}, i_{mq}	dq-axis currents of the motor drive unit.
L_d, L_q	dq-axis stator inductances.
L_m, L_e	Filter inductances.
L_s	Stator average inductance.
R_d	Filter damping resistance.
R_m, R_e	Internal resistances of L_m and L_e.
T_s	Sampling time of the EME.
u_{cd}, u_{cq}	dq-axis voltages of the filter capacitance.
u_{ed}, u_{eq}	dq-axis voltages of the emulating converter.
u_{ld}, u_{lq}	dq-axis disturbance voltages.
u_{md}, u_{mq}	dq-axis voltages of the motor drive unit.

The associate editor coordinating the review of this manuscript and approving it for publication was Akshay Kumar Saha.

I. INTRODUCTION

The electric machine emulator (EME), based on power hardware-in-the-loop (PHIL) technology, can emulate the characteristics of actual machines with different types/ratings [1], [2]. Compared with HIL test, the EME can exchange high-power energy with motor drive unit (MDU) in addition to logic and control signals [2], [3]. Besides, the EME can achieve much easier and safer fault configuration than dynamometer test. Therefore, EMEs have attracted extensive attention in electric vehicles [4], [5], wind power [6] and smart grids [7]. Several EMEs have been developed for industrial machines, such as induction machines [8], [9],

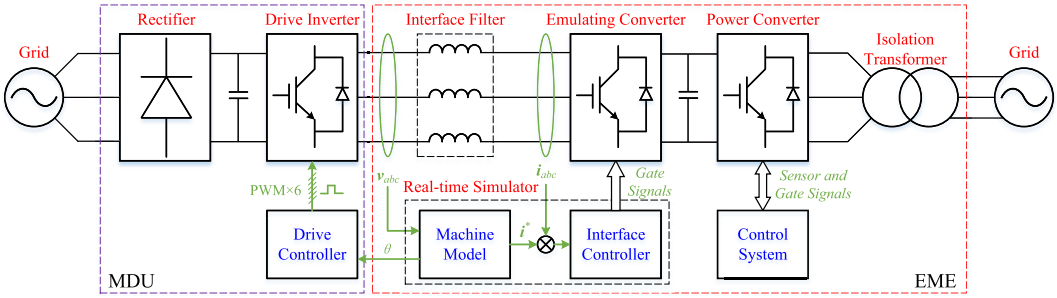

FIGURE 1. Typical EME schematic diagram for MDU testing.

permanent magnet synchronous machines (PMSMs) [2], [5], [10], brushless DC motors [11], [12], and switched reluctance machines [13]. As shown in Fig. 1, a typical EME consists of the interface filter (IF), emulating converter (EC), real-time simulator (RTS), power supply and sampling circuits [5], [8]. In the RTS, the machine model takes the terminal voltages of the MDU as input and calculates the reference currents as output to the interface controller. Then, the command voltages of the EC are calculated, and the actual currents are reached by controlling the terminal voltages of the IF.

Emulating accuracy is the key concern since the EME is used to replace the actual machine to test and validate the performance of the MDU [14]. As the controlled main component, the IF is not only used for harmonic suppression, but also determines the structure of the interface control algorithm (ICA) and system bandwidth. Therefore, the IF is of great significance to the emulating accuracy. Three types of IFs have been presented in EMEs, namely, L, LC and LCL filters [4], [15]. Among them, the LC filter may only be found in generator emulators [16], [17] despite better filtering capability than the L filter. The main reason is that the LC filter is asymmetric, which cannot be applied to the EME operating in four quadrants.

The L filter has been most widely used in EMEs. The main advantage of the L filter is that a simple linear proportional-integral (PI) controller can be adopted as the ICA since it is a first-order system. EMEs based on PI controller have been developed in [8], [12], [18], [19], in which acceptable accuracy can be reached in the low-frequency region, whereas the dynamic performance in the high-frequency region is distorted because the low-pass filter (LPF) characteristic of the PI controller narrows system bandwidth [20]. In [10], feedforward control is added to the PI controller to extend system bandwidth, but the problem has not been thoroughly overcome. Besides, as shown in Fig. 1, control conflicts may arise due to the same currents being controlled by both the MDU and EME. To avoid the conflicts, [5] recommends that the current loop bandwidth of the EME needs to be at least five times higher than that of the MDU, which may impose a high cost and demand for the EME.

Open-loop current control (OLCC) has also been proposed for L filter-based EME [21], in which the command voltages of the EC are directly calculated through the machine and IF models, thus resolving control conflicts and improving

TABLE 1. Comparison of the existing EMEs and the proposed EME.

Literatures	IFs	ICAs	Deficiency	Improvements in this paper
In [5], [18]	L filter	PI	Control conflicts, limited bandwidth	LCL filter +DDPCC
In [9]	L filter+ linear amp.	PI+lead-lag compensator	Control conflicts, high losses, limited power	LCL filter+ switching device based converter
In [15]	LCL filter	LQR	Trial-error based design, varying ac errors, poor robustness	DQ-frame-based DDPCC+UIOs +unified design
In [16], [17]	LC filter	Dual PI	Unidirectional energy flow	LCL filter
In [20], [22]	L filter	OLCC	Poor robustness	Closed-loop DDPCC
In [24]	LCL filter	MPC	Trial-error based design, varying ac errors, poor stability and robustness	DQ-frame-based DDPCC+UIOs+ stability analysis +unified design

dynamic response. In [22] and [20], an OLCC based on direct impedance regulation is presented, where the differential operation is eliminated to improve robustness. Nevertheless, the accuracy of the EME based on open-loop control deeply depends on accurate modeling and hardware implementation. Thus, unacceptable deviations from the actual machine may occur due to inevitable modeling errors and nonlinearities of the converter. Also, the inductance of the L filter can only be adjusted within a limited range since small values are ideal for high bandwidth while higher values are more effective for harmonic suppression [23], which further compromises the emulating accuracy and hinders its application.

The LCL filter seems to be the most suitable IF for EME. It can completely eliminate control conflicts because the addition of the capacitor branch decouples the current loop of the EME from that of the MDU [5]. Also, the performance of the PHIL system with the L and LCL filters is compared in [23], concluding that the LCL filter is better both in time domain and frequency domain. However, there are few EME literatures involving LCL filter due to its complex structure and cumbersome control. In [24], the EME with LCL filter is presented to test the performance of the inverter for elevator applications, in which a predictive algorithm is directly deduced based on backward difference and model inversion. Moreover, the LCL filter-based load emulator is proposed in [15], where the linear quadratic regulator (LQR) based on state feedback control is designed to improve the transient

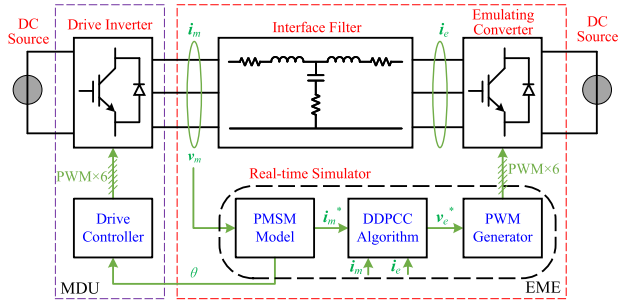

FIGURE 2. Overall schematic of the proposed EME based on LCL filter.

response. Nevertheless, both aforementioned ICAs are developed in *abc* frame, which not only introduces time-varying ac errors but also requires higher-bandwidth controller. Meanwhile, these algorithms suffer from a common problem that inevitable adverse factors such as the resonance, time delay and parameter uncertainty are not taken into account, leading to poor robustness and stability. In addition, unlike in grid-connected systems [25], [26], the LCL filter in EMEs have an impact not only on harmonic suppression, but also on system stability and bandwidth. Yet, there is no universal method presented for the parameter design of the LCL filter in EMEs.

In this paper, the LCL filter with passive damping is chosen as the IF. The comparison of the existing EMEs and the proposed EME is presented in Table 1, and the main contributions of this paper are further detailed as follows.

1) A dual closed-loop deadbeat predictive current control (DDPCC) based on *dq* frame is proposed, which effectively improves the dynamic accuracy of the EME. Also, the parameter constraints obtained based on the analysis in the discrete domain ensure the system stability, thereby further improving the practicability of the algorithm.
2) The parameter sensitivity of the ICA is analyzed in detail. On this basis, two unknown input observers (UIOs) are designed to compensate for the disturbance currents and voltages introduced by modeling errors. Thus, the system robustness is considerably enhanced.
3) A universal approach based on theoretical analysis rather than engineering experience is proposed, which comprehensively considers the harmonic suppression, bandwidth, stability and resonance.

Therefore, the proposed EME takes the emulating accuracy, stability and robustness into account, so that it is operative for various complex working conditions. The rest of this paper is structured as follows. Section II presents a detailed design and in-depth analysis for the EME. Sections III and IV are to validate the proposed EME through simulations and experiments, respectively. Section V concludes this paper.

II. DESIGN AND ANALYSIS OF THE EME

The overall schematic of the proposed EME in this paper is shown in Fig. 2. Compared with Fig. 1, the MDU and

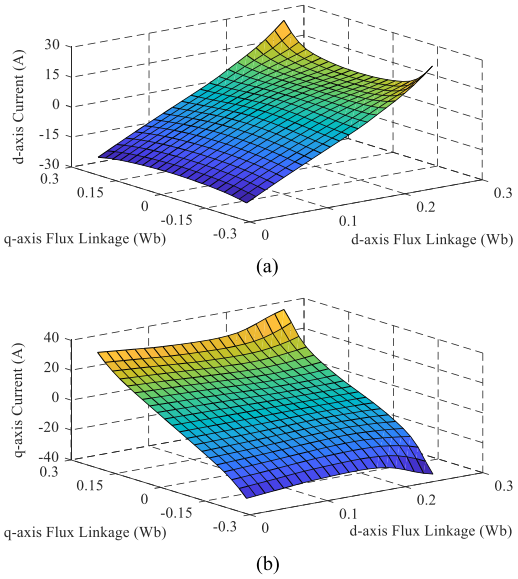

FIGURE 3. Current maps versus d- and q-axis flux linkages at 0° rotor position. (a) d-axis current. (b) q-axis current.

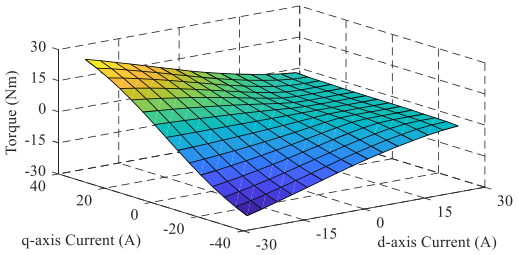

FIGURE 4. Torque maps versus d- and q-axis currents at 0° rotor position.

EME are powered by two independent DC sources instead of the rectifier or power converter. Besides, the LCL filter with passive damping is chosen as the IF, and a high-bandwidth DDPCC is proposed as the ICA to improve dynamic performance of the EME. In addition, the PMSM is selected as the target motor to be emulated in this paper, for it is widely used in electric drive systems due to high efficiency, high power density and small size.

A. MACHINE MODEL

The accuracy of the machine model has a significant impact on the emulating accuracy. Various machine models, including mathematical models and look-up tables based models extracted from finite element analysis (FEA), have been implemented in real-time systems. Mathematical models are popular in electric drives due to their low computational effort, but the nonlinear characteristics of the machine cannot be taken into account. In this paper, a high-fidelity and computationally efficient look-up tables based machine model presented in [27] is used, which considers both the magnetic saturation and spatial harmonics.

For the aforementioned machine model, the flux linkage and torque functions of d- and q-axis currents and the rotor position are initially extracted by the FEA for a prototype PMSM. Subsequently, the current maps versus d- and q-axis

flux linkages at different rotor positions are obtained by the inverse solution [27]. The resultant look-up tables of d- and q-axis currents and torque at 0° rotor position are shown in Figs. 3 and 4.

B. PROPOSED INTERFACE CONTROL ALGORITHM

The system bandwidth not only affects the dynamic accuracy, but also determines the performance of the EME at high operating speed. Considering the multi-pole characteristic of the LCL filter, linear PI control is no longer applicable since very limited bandwidth is available. Besides, the dynamic performance will be distorted at high operating speed due to the LPF characteristic, which further narrows the operating speed range. As the predictive control with high bandwidth is excellent for controlling multiple-input multiple-output systems, a novel DDPCC-based ICA in dq frame is proposed to reach an accurate emulation.

1) DYNAMIC EQUATION OF THE INTERFACE FILTER

For simplicity, the single-phase LCL filter shown in Fig. 5 is initially analyzed. The dynamic equation of the single-phase filter is derived as follows.

$$\begin{cases} u_m = (R_m + R_d)i_m + L_m\dfrac{di_m}{dt} + u_c - R_d i_e \\ u_e = -(R_e + R_d)i_e - L_e\dfrac{di_e}{dt} + u_c + R_d i_m \\ C\dfrac{du_c}{dt} = i_m - i_e \end{cases} \tag{1}$$

Equation (1) is subsequently extended and transformed to dq frame by Park transform as follows.

$$\begin{cases} u_{md} = (R_m + R_d)i_{md} + L_m\dfrac{di_{md}}{dt} - \omega_e L_m i_{mq} \\ \qquad +u_{cd} - R_d i_{ed} \\ u_{mq} = (R_m + R_d)i_{mq} + L_m\dfrac{di_{mq}}{dt} + \omega_e L_m i_{md} \\ \qquad +u_{cq} - R_d i_{eq} \end{cases} \tag{2}$$

$$\begin{cases} u_{ed} = -(R_e + R_d)i_{ed} - L_e\dfrac{di_{ed}}{dt} + \omega_e L_e i_{eq} \\ \qquad +u_{cd} + R_d i_{md} \\ u_{eq} = -(R_e + R_d)i_{eq} - L_e\dfrac{di_{eq}}{dt} - \omega_e L_e i_{ed} \\ \qquad +u_{cq} + R_d i_{mq} \end{cases} \tag{3}$$

According to (2) and (3), the currents $\boldsymbol{i}_m = \begin{bmatrix} i_{md} & i_{mq} \end{bmatrix}^{\mathrm{T}}$ flowing through the MDU is not directly regulated by the terminal voltages $\boldsymbol{u}_e = \begin{bmatrix} u_{ed} & u_{eq} \end{bmatrix}^{\mathrm{T}}$, but controlled by the currents $\boldsymbol{i}_e = \begin{bmatrix} i_{ed} & i_{eq} \end{bmatrix}^{\mathrm{T}}$ flowing through the EC. Inspired by the idea of backstepping control, in which the complex nonlinear control system is decomposed into several subsystems by introducing virtual control variables [28], [29], the current control of the LCL filter-based EME can also be decomposed into two simple subsystems, one to adjust the currents $\boldsymbol{i}_m$ to track the reference ones $\boldsymbol{i}_m^*$ by accurately calculating the desired currents $\boldsymbol{i}_e^*$, and the other to force the currents $\boldsymbol{i}_e$ to track the desired by exactly controlling

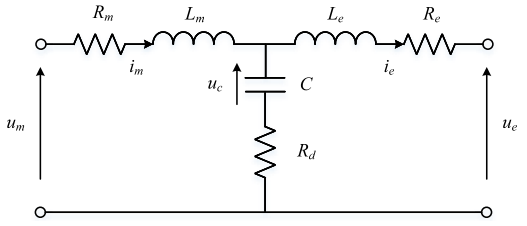

FIGURE 5. Schematic of the single-phase LCL filter.

the command voltages $\boldsymbol{u}_e^*$. That is to say, the currents $\boldsymbol{i}_e^*$ are selected as the intermediate control variables. However, different from backstepping control, the control law here can be directly derived without constructing the Lyapunov function since the system described by (2) and (3) is linear. In other words, derivative operations, Lyapunov function calculations, and complex gain tuning are all avoided. Thus, the proposed algorithm is computationally efficient and easy to implement.

2) DPCC FOR THE CURRENTS FLOWING THROUGH THE MDU

The prediction equation of the currents flowing through the MDU is obtained by forward Euler discretization of (2) as

$$\boldsymbol{i}_{m,k+1} = \boldsymbol{A}_m\boldsymbol{i}_{m,k} + \boldsymbol{B}_m(\boldsymbol{u}_{m,k} - \boldsymbol{u}_{c,k}) + \boldsymbol{C}_m\boldsymbol{i}_{e,k} \tag{4}$$

where

$$\boldsymbol{A}_m = \begin{bmatrix} 1 - \frac{T_s(R_m+R_d)}{L_m} & \omega_{e,k}T_s \\ -\omega_{e,k}T_s & 1 - \frac{T_s(R_m+R_d)}{L_m} \end{bmatrix}$$

$$\boldsymbol{B}_m = \begin{bmatrix} \frac{T_s}{L_m} & 0 \\ 0 & \frac{T_s}{L_m} \end{bmatrix}, \boldsymbol{C}_m = \begin{bmatrix} \frac{T_s R_d}{L_m} & 0 \\ 0 & \frac{T_s R_d}{L_m} \end{bmatrix}$$

and $\boldsymbol{u}_{m,k} = \begin{bmatrix} u_{md,k} & u_{mq,k} \end{bmatrix}^{\mathrm{T}}$, $\boldsymbol{u}_{c,k} = \begin{bmatrix} u_{cd,k} & u_{cq,k} \end{bmatrix}^{\mathrm{T}}$.

For deadbeat control, the predictive currents are assumed to be equal to the references output by the machine model as

$$\boldsymbol{i}_{m,k+1} = \boldsymbol{i}_{m,k}^*. \tag{5}$$

According to (4) and (5), the reference currents flowing through the EC can be derived as

$$\boldsymbol{i}_{e,k}^* = \boldsymbol{C}_m^{-1}[\boldsymbol{i}_{m,k}^* - \boldsymbol{A}_m\boldsymbol{i}_{m,k} - \boldsymbol{B}_m(\boldsymbol{u}_{m,k} - \boldsymbol{u}_{c,k})]. \tag{6}$$

3) DPCC FOR THE CURRENTS FLOWING THROUGH THE EC

Similarly, the prediction equation of the currents flowing through the EC is derived by discretizing (3) as

$$\boldsymbol{i}_{e,k+1} = \boldsymbol{A}_e\boldsymbol{i}_{e,k} + \boldsymbol{B}_e(\boldsymbol{u}_{c,k} - \boldsymbol{u}_{e,k}) + \boldsymbol{C}_e\boldsymbol{i}_{m,k} \tag{7}$$

where

$$\boldsymbol{A}_e = \begin{bmatrix} 1 - \frac{T_s(R_e+R_d)}{L_e} & \omega_{e,k}T_s \\ -\omega_{e,k}T_s & 1 - \frac{T_s(R_e+R_d)}{L_e} \end{bmatrix}$$

$$\boldsymbol{B}_e = \begin{bmatrix} \frac{T_s}{L_e} & 0 \\ 0 & \frac{T_s}{L_e} \end{bmatrix}, \boldsymbol{C}_e = \begin{bmatrix} \frac{T_s R_d}{L_e} & 0 \\ 0 & \frac{T_s R_d}{L_e} \end{bmatrix}.$$

Likewise, the following assumption is established.

$$\boldsymbol{i}_{e,k+1} = \boldsymbol{i}_{e,k}^* \tag{8}$$

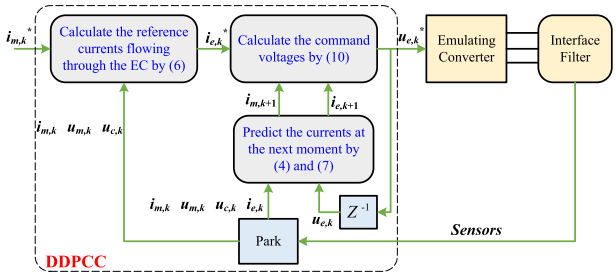

FIGURE 6. Diagram of the proposed DDPCC with delay compensation.

According to (7) and (8), the command voltages of the EC can be expressed as

$$\boldsymbol{u}^*_{e,k} = \boldsymbol{B}_e^{-1}(-\boldsymbol{i}^*_{e,k} + \boldsymbol{A}_e\boldsymbol{i}_{e,k} + \boldsymbol{C}_e\boldsymbol{i}_{m,k}) + \boldsymbol{u}_{c,k}. \tag{9}$$

4) DELAY COMPENSATION

In practice, the terminal voltages obtained at current moment will be applied at next moment, which may weaken the robustness of the algorithm. Thus, the delay should be compensated, and the voltage equation is accordingly updated as

$$\boldsymbol{u}^*_{e,k} = \boldsymbol{B}_e^{-1}(-\boldsymbol{i}^*_{e,k} + \boldsymbol{A}_e\boldsymbol{i}_{e,k+1} + \boldsymbol{C}_e\boldsymbol{i}_{m,k+1}) + \boldsymbol{u}_{c,k+1} \tag{10}$$

where $\boldsymbol{i}_{m,k+1}$ and $\boldsymbol{i}_{e,k+1}$ are calculated by (4) and (7), respectively. In addition, considering the time constant of the capacitance is much larger than that of the inductance due to the presence of the damping resistance, $\boldsymbol{u}_{c,k+1} \approx \boldsymbol{u}_{c,k}$ is established when the sampling time is short enough.

As a result, the diagram of the proposed DDPCC with delay compensation is shown in Fig. 6, where the reference currents $\boldsymbol{i}^*_{m,k}$ flowing through the MDU are initially derived from machine model (see Fig. 2), and subsequently, the reference currents $\boldsymbol{i}^*_{e,k}$ flowing through the EC are calculated by (6) based on $\boldsymbol{i}^*_{m,k}$ and the variables measured by sensors. Simultaneously, the currents $\boldsymbol{i}_{m,k+1}$ and $\boldsymbol{i}_{e,k+1}$ are predicted by (4) and (7), respectively, to compensate for the unit delay. These variables are then entered into (10) to calculate the command voltages $\boldsymbol{u}^*_{e,k}$, which will be ultimately modulated by PWM generator to drive the converter (see Fig. 2).

C. STABILITY ANALYSIS

System stability is a prerequisite for the operation of the EME. For the backstepping control, the system stability is ensured by constructing the Lyapunov function while obtaining the control law. However, the proposed DDPCC algorithm is directly deduced based on the linear system described by (2) and (3), so inappropriate system parameters may lead to a remarkable increase in prediction errors and thus cause system instability. Moreover, since the LCL filter is a third-order system, the unexpected resonance may cause further augmented prediction errors, thus increasing the tendency of system instability. Therefore, this section presents a detailed stability analysis, and the constraints on system parameters are obtained accordingly.

As shown in Fig. 6, the terminal voltages $\boldsymbol{u}_m$ of the MDU are sampled to calculate the predictive currents along with desired currents $\boldsymbol{i}^*_e$. According to Shannon sampling theorem, the sampling time of the EME needs to be at least twice as high as that of the MDU. In fact, the sampling time of the EME is typically three to five times higher than that of the MDU to reach an accurate emulation, which means T_s is quite small. In this case, [30] indicates that the cross-coupling term $\omega_e T_s$ has little impact on system stability. To explain it, the tracking errors of the outer- and inner-loop controllers are defined as

$$\begin{cases} z_1 = i_{md} - i^*_{md} \\ z_2 = i_{mq} - i^*_{mq} \\ z_3 = i_{ed} - i^*_{ed} \\ z_4 = i_{eq} - i^*_{eq}. \end{cases} \tag{11}$$

Based on (2) and (11), we can get

$$\begin{aligned} \dot{z}_1 = &-\frac{R_m + R_d}{L_m} i_{md,t} + \frac{1}{L_m}(u_{md,t} - u_{cd,t}) \\ &+\omega_{e,t} i_{mq,t} + \frac{R_d}{L_m}(i^*_{ed,k} + z_3) - \dot{i}^*_{md,k} \end{aligned} \tag{12}$$

where $t \in [k, k+1]$. When the sampling time T_s is small enough ($T_s \ll 1/\omega_e$), it is reasonable for low- and medium-speed emulated motors to suppose that the system variables, except for the pulsewidth voltage u_{md}, remain constant in one control cycle, i.e., $i_{md,t} = i_{md,k}$, $i_{mq,t} = i_{mq,k}$, and $\omega_{e,t} = \omega_{e,k}$. On this basis, (12) can be simplified as (13) by substituting (6) into it.

$$\dot{z}_1 = -\frac{1}{T_s} z_1 + \frac{R_d}{L_m} z_3 + \frac{1}{L_m}(u_{md,t} - u_{md,k}) - \dot{i}^*_{md,k} \tag{13}$$

Obviously, the cross-coupling term $\omega_{e,t} i_{mq,t}$ is cancelled out by the control term $\omega_{e,k} i_{mq,k}$ in $\dot{z}_1$, as well as in $\dot{z}_2$. Taking the outer current loop in Fig. 6 as an example, when the Lyapunov function is designed as $V_1 = z_1^2/2 + z_2^2/2$, the resultant $\dot{V}_1 = z_1\dot{z}_1 + z_2\dot{z}_2$ clearly does not contain cross-coupling term, which means that this term has almost no effect on system stability. It should be noted that this conclusion still holds for other forms of Lyapunov functions since V_1 is positive definite throughout. The same finding can be obtained from the inner current loop. Furthermore, according to (13), it may be difficult to directly acquire stability conditions since constructing the proper Lyapunov function is cumbersome. Actually, according to the expressions of coefficient matrices $\boldsymbol{A}_m, \boldsymbol{B}_m, \boldsymbol{C}_m, \boldsymbol{A}_e, \boldsymbol{B}_e$, and $\boldsymbol{C}_e$, the system can be considered as a single-input single-output one by ignoring the cross-coupling term, which contributes to a simpler analysis method. In this way, coefficient matrices can be simplified as

$$\begin{aligned} a_m &= 1 - \frac{T_s(R_m + R_d)}{L_m}, b_m = \frac{T_s}{L_m}, c_m = \frac{T_s R_d}{L_m}, \\ a_e &= 1 - \frac{T_s(R_e + R_d)}{L_e}, b_e = \frac{T_s}{L_e}, c_e = \frac{T_s R_d}{L_e}. \end{aligned} \tag{14}$$

The voltage equation with $\boldsymbol{i}^*_{m,k}$ as input can be expressed as (15) by substituting (4), (6), (7) and (14) into (10).

$$\boldsymbol{u}^*_{o,k} = b_e^{-1}(c_m^{-1}\boldsymbol{i}^*_{m,k} - p_m\boldsymbol{i}_{m,k} - q_m\boldsymbol{u}_{i,k} - p_e\boldsymbol{i}_{e,k} - q_e\boldsymbol{u}_{o,k}) \tag{15}$$

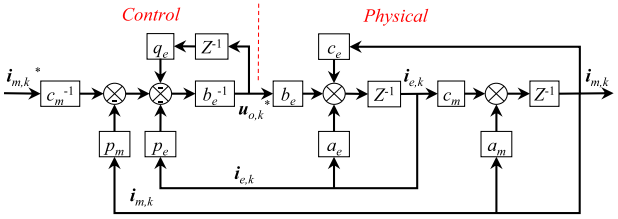

FIGURE 7. Block diagram of the EME current loop.

where

$$\begin{cases} \boldsymbol{u}_{i,k} = \boldsymbol{u}_{m,k} - \boldsymbol{u}_{c,k} \\ \boldsymbol{u}_{o,k} = \boldsymbol{u}_{c,k} - \boldsymbol{u}_{e,k} \\ \boldsymbol{u}_{o,k}^* = \boldsymbol{u}_{c,k+1} - \boldsymbol{u}_{e,k}^* \end{cases} \tag{16}$$

$$\begin{cases} p_m = (c_m^{-1} + c_e)a_m + a_e c_e \\ q_m = (c_m^{-1} + c_e)b_m \\ p_e = c_m c_e + {a_e}^2 \\ q_e = a_e b_e. \end{cases} \tag{17}$$

According to (15), the block diagram of the EME current loop is shown in Fig. 7, where the EC is assumed to be an ideal component and $\boldsymbol{u}_{i,k}$ is neglected for simplicity as it has no effect on the analysis. Subsequently, the transfer function from $\boldsymbol{i}_{m,k}^*$ to $\boldsymbol{i}_{m,k}$ can be obtained as

$$G(z) = \frac{z}{a_3 z^3 + a_2 z^2 + a_1 z + a_0} \tag{18}$$

where

$$\begin{cases} a_0 = a_e(a_m a_e - c_m c_e) \\ a_1 = a_m + (a_e - 1)c_m c_e - (1 + a_m){a_e}^2 \\ a_2 = {a_e}^2 - a_m + c_m c_e \\ a_3 = 1. \end{cases} \tag{19}$$

According to Jury criterion for discrete system, the stability conditions can be expressed as

$$\begin{cases} A(1) = a_3 + a_2 + a_1 + a_0 > 0 \\ -A(-1) = a_3 - a_2 + a_1 - a_0 > 0 \\ a_3 > |a_0| \\ {a_3}^2 - {a_0}^2 > a_3 a_1 - a_2 a_0 \end{cases} \tag{20}$$

where $A(z) = a_3 z^3 + a_2 z^2 + a_1 z + a_0$.

As described in Section II-E, the parameters of the LCL filter satisfy $L_m = L_e$ and $R_m = R_e$, which means

$$a_m = a_e, \quad b_m = b_e, \quad c_m = c_e. \tag{21}$$

Furthermore, considering $R_m \ll R_d$, the following relationship is satisfied.

$$a_m + c_m \approx 1 \tag{22}$$

Based on (21) and (22), the stability conditions can be rewritten as

$$\begin{cases} A(1) = 1 > 0 \\ -A(-1) = -1 + 8a_m - 8{a_m}^2 > 0 \\ 1 + a_m - 2{a_m}^2 > 0 \\ 2 - 5a_m + 8{a_m}^2 - 4{a_m}^3 > 0. \end{cases} \tag{23}$$

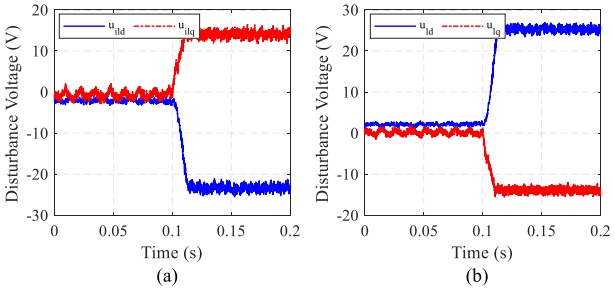

FIGURE 8. Simulation results of disturbance voltages under $R_d = 2R_d^{real}$. (a) u_{ild} and u_{ilq}. (b) u_{ld} and u_{lq}.

Eventually, the constraints is obtained by solving (23) as

$$0.146 < \frac{T_s R_d}{L_m} < 0.854. \tag{24}$$

According to (24), when the sampling time T_s is determined, the damping resistance R_d should take on a value that is proportional to the inductance L_m in order to achieve a stable operation. In other words, as the inductance increases, a larger damping resistance is required to ensure stability.

It should be noted that the above conclusion is obtained by simplifying the system to a single-input single-output one based on the premise that $i_{mq,t}$ and $\omega_{e,t}$ remain constant within each control period. For low- and medium-speed motors, it is completely operative due to the large mechanical time constant and large stator inductance. However, this premise will no longer hold for high-speed motors ($T_s \ll 1/\omega_e$ is not satisfied) with the smaller inductance. For instance, for $T_s = 20\ \mu$s in this paper, when $\omega_e > 5000$ rad/s (i.e., 796 Hz in the electrical frequency and $\omega_e T_s > 0.1$), the previous analysis may not be applicable. In this case, it may be more straightforward to resolve the stability conditions by constructing a proper Lyapunov function.

D. DISTURBANCE ANALYSIS AND SUPPRESSION

Since the proposed DDPCC is a model-based control method, the performance largely depends on the modeling accuracy of the IF. However, the IF is subject to parameter variation and uncertainty. For instance, the inductance decreases as the current rises, and the resistance increases as the temperature rises. According to (4), (6), and (7), the prediction and reference current errors caused by parameter mismatch can be represented based on the deviation matrices $\Delta\boldsymbol{A}_m$, $\Delta\boldsymbol{B}_m$, $\Delta\boldsymbol{C}_m$, $\Delta\boldsymbol{A}_e$, $\Delta\boldsymbol{B}_e$ and $\Delta\boldsymbol{C}_e$ as (25), (26), and (27), as shown at the bottom of the next page, respectively.

$$\Delta\boldsymbol{i}_{m,k+1} = \Delta\boldsymbol{A}_m\boldsymbol{i}_{m,k} + \Delta\boldsymbol{B}_m\boldsymbol{u}_{i,k} + \Delta\boldsymbol{C}_m\boldsymbol{i}_{e,k} \tag{25}$$

$$\Delta\boldsymbol{i}_{e,k+1} = \Delta\boldsymbol{A}_e\boldsymbol{i}_{e,k} + \Delta\boldsymbol{B}_e\boldsymbol{u}_{o,k} + \Delta\boldsymbol{C}_e\boldsymbol{i}_{m,k} \tag{26}$$

where $\boldsymbol{u}_i$, $\boldsymbol{u}_o$ are defined as (16).

As shown in Fig. 6, the prediction and reference current errors do not directly affect the emulating accuracy, but indirectly through the command voltages $\boldsymbol{u}_e^*$. Therefore, it is necessary to derive the command voltage errors for further analysis. According to (10), the exact command voltages

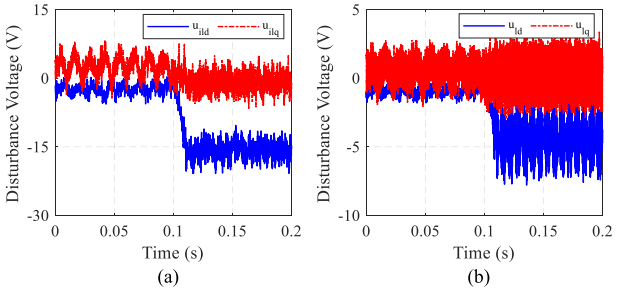

FIGURE 9. Simulation results of disturbance voltages under $L_m = 2L_m^{real}$ and $L_e = 2L_e^{real}$. (a) u_{ild} and u_{ilq}. (b) u_{ld} and u_{lq}.

under parameter mismatch can be expressed as (28), shown at the bottom of the page. Further, the voltage errors can be derived as (29), shown at the bottom of the page, by substracting (10) from (28). Clearly, the errors can be divided into two parts, one is the error (defined as $\boldsymbol{u}_{il}$) caused by the aforementioned disturbance currents (i.e., $\Delta\boldsymbol{i}^*_{e,k}$, $\Delta\boldsymbol{i}_{e,k+1}$ and $\Delta\boldsymbol{i}_{m,k+1}$), and the other comes from the disturbance voltages (defined as $\boldsymbol{u}_l$) generated by parameter mismatch (i.e., $\Delta\boldsymbol{A}_e$, $\Delta\boldsymbol{B}_e$ and $\Delta\boldsymbol{C}_e$) alone. As a result, the parameter mismatch initially introduces the disturbance currents, which in turn acts on the command voltages along with the disturbance voltages, thus deteriorating the emulating accuracy.

Figs. 8 and 9 quantitatively evaluate the effect of the parameter mismatch on the disturbance voltages, where the desired currents $\boldsymbol{i}^*_m$ are set as $[i^*_{md}, i^*_{mq}] = [0, 5]$ A, and the motor speed is stepped from 20 Hz to 150 Hz at 0.1 s. The rest of the configurations are the same as in Section III. As can be seen, the disturbance voltages caused by both resistance mismatch and inductance mismatch rise dramatically as the speed increases, indicating that disturbance suppression is crucial especially for high-speed operation. Moreover, the resistance mismatch only causes the offset errors, while the inductance mismatch not only produces the offset errors, but also leads to the violent fluctuation in disturbance voltages, which means that the waveform quality of the controlled currents will also deteriorate under the inductance mismatch.

Indeed, (29) also specifies the direction of disturbance rejection that we can counteract $\boldsymbol{u}_{il}$ by compensating for disturbance currents, while offsetting disturbance voltages $\boldsymbol{u}_l$ to completely eliminate the errors. Various disturbance estimation and attenuation methods have been developed, such as extended state observer [31], finite-time disturbance observer [29], nonlinear disturbance observer [32]–[34],

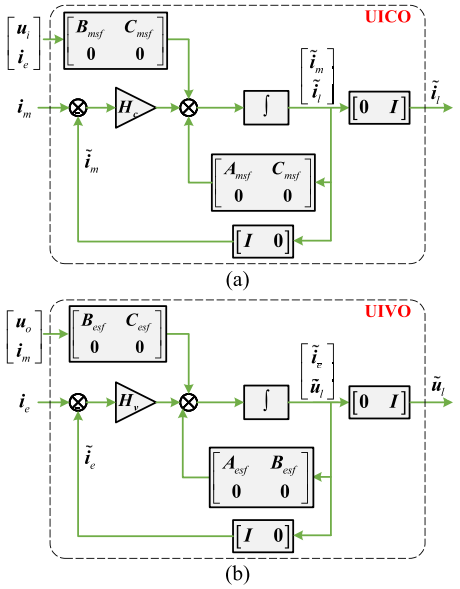

FIGURE 10. Block diagrams of the proposed disturbance observers. (a) UICO. (b) UIVO.

and UIO [35], [36]. For these approaches, the estimated lumped disturbances are employed for feedforward compensation control. Among them, the UIO, integrating state feedback and disturbance evaluation, has become one of the most extensively investigated and applied methods due to its excellent ability to suppress disturbances and uncertainties. Therefore, the UIO is adopted here, and unknown input current observer (UICO) and unknown input voltage observer (UIVO) are presented to compensate for the disturbance currents and voltages, respectively.

Based on (2) and (3), the state-space form of the IF model can be derived as

$$\dot{\boldsymbol{i}}_m = \boldsymbol{A}_{ms}\boldsymbol{i}_m + \boldsymbol{B}_{ms}\boldsymbol{u}_i + \boldsymbol{C}_{ms}\boldsymbol{i}_e \tag{30}$$

$$\dot{\boldsymbol{i}}_e = \boldsymbol{A}_{es}\boldsymbol{i}_e + \boldsymbol{B}_{es}\boldsymbol{u}_o + \boldsymbol{C}_{es}\boldsymbol{i}_m \tag{31}$$

where

$$\boldsymbol{A}_{ms} = \begin{bmatrix} -\frac{R_m+R_d}{L_m} & \omega_e \\ -\omega_e & \frac{R_m+R_d}{L_m} \end{bmatrix}, \quad \boldsymbol{B}_{ms} = \begin{bmatrix} \frac{1}{L_m} & 0 \\ 0 & \frac{1}{L_m} \end{bmatrix},$$

$$\boldsymbol{A}_{es} = \begin{bmatrix} -\frac{R_e+R_d}{L_e} & \omega_e \\ -\omega_e & \frac{R_e+R_d}{L_e} \end{bmatrix}, \quad \boldsymbol{B}_{es} = \begin{bmatrix} \frac{1}{L_e} & 0 \\ 0 & \frac{1}{L_e} \end{bmatrix},$$

$$\Delta\boldsymbol{i}^*_{e,k} = \Delta\boldsymbol{C}_m^{-1}\boldsymbol{i}^*_{m,k} - (\Delta\boldsymbol{A}_m\boldsymbol{C}_m^{-1} + \boldsymbol{A}_m\Delta\boldsymbol{C}_m^{-1} + \Delta\boldsymbol{A}_m\Delta\boldsymbol{C}_m^{-1})\boldsymbol{i}_{m,k} - (\Delta\boldsymbol{B}_m\boldsymbol{C}_m^{-1} + \boldsymbol{B}_m\Delta\boldsymbol{C}_m^{-1} + \Delta\boldsymbol{B}_m\Delta\boldsymbol{C}_m^{-1})\boldsymbol{u}_{i,k} \tag{27}$$

$$\boldsymbol{u}^*_{e,k} = (\boldsymbol{B}_e^{-1} + \Delta\boldsymbol{B}_e^{-1})\left[-(\boldsymbol{i}^*_{e,k} + \Delta\boldsymbol{i}^*_{e,k}) + (\boldsymbol{A}_e + \Delta\boldsymbol{A}_e)(\boldsymbol{i}_{e,k+1} + \Delta\boldsymbol{i}_{e,k+1}) + (\boldsymbol{C}_e + \Delta\boldsymbol{C}_e)(\boldsymbol{i}_{m,k+1} + \Delta\boldsymbol{i}_{m,k+1})\right] + \boldsymbol{u}_{c,k} \tag{28}$$

$$\Delta\boldsymbol{u}^*_{e,k} = \overbrace{(\boldsymbol{B}_e^{-1} + \Delta\boldsymbol{B}_e^{-1})\left[-\Delta\boldsymbol{i}^*_{e,k} + (\boldsymbol{A}_e + \Delta\boldsymbol{A}_e)\Delta\boldsymbol{i}_{e,k+1} + (\boldsymbol{C}_e + \Delta\boldsymbol{C}_e)\Delta\boldsymbol{i}_{m,k+1}\right]}^{\boldsymbol{u}_{il}}$$
$$+ \underbrace{\left[-\Delta\boldsymbol{B}_e^{-1}\boldsymbol{i}^*_{e,k} + (\boldsymbol{A}_e\Delta\boldsymbol{B}_e^{-1} + \Delta\boldsymbol{A}_e\boldsymbol{B}_e^{-1} + \Delta\boldsymbol{A}_e\Delta\boldsymbol{B}_e^{-1})\boldsymbol{i}_{e,k+1} + (\Delta\boldsymbol{B}_e^{-1}\boldsymbol{C}_e + \boldsymbol{B}_e^{-1}\Delta\boldsymbol{C}_e + \Delta\boldsymbol{B}_e^{-1}\Delta\boldsymbol{C}_e)\boldsymbol{i}_{m,k+1}\right]}_{\boldsymbol{u}_l} \tag{29}$$

$$\boldsymbol{C}_{ms} = \begin{bmatrix} \frac{R_d}{L_m} & 0 \\ 0 & \frac{R_d}{L_m} \end{bmatrix}, \quad \boldsymbol{C}_{es} = \begin{bmatrix} \frac{R_d}{L_e} & 0 \\ 0 & \frac{R_d}{L_e} \end{bmatrix}.$$

The UICO is first designed to compensate for disturbance currents to eliminate $\boldsymbol{u}_{il}$. Considering the errors between the reference model and the actual model, the deviation matrices $\Delta\boldsymbol{A}_{ms}$, $\Delta\boldsymbol{B}_{ms}$, and $\Delta\boldsymbol{C}_{ms}$ can be defined as

$$\begin{cases} \boldsymbol{A}_{ms} = \boldsymbol{A}_{msf} + \Delta\boldsymbol{A}_{ms} \\ \boldsymbol{B}_{ms} = \boldsymbol{B}_{msf} + \Delta\boldsymbol{B}_{ms} \\ \boldsymbol{C}_{ms} = \boldsymbol{C}_{msf} + \Delta\boldsymbol{C}_{ms} \end{cases} \tag{32}$$

where $\boldsymbol{A}_{msf}$, $\boldsymbol{B}_{msf}$, and $\boldsymbol{C}_{msf}$ are the coefficient matrices of the reference model.

The dynamic equation with modeling errors can be obtained by substituting (32) into (30) as

$$\begin{aligned} \dot{\boldsymbol{i}}_m = {} & \boldsymbol{A}_{msf}\boldsymbol{i}_m + \boldsymbol{B}_{msf}\boldsymbol{u}_i + \boldsymbol{C}_{msf}\boldsymbol{i}_e \\ & + \Delta\boldsymbol{A}_{ms}\boldsymbol{i}_m + \Delta\boldsymbol{B}_{ms}\boldsymbol{u}_i + \Delta\boldsymbol{C}_{ms}\boldsymbol{i}_e \end{aligned} \tag{33}$$

and the terms involving the model errors can be considered as unknown input disturbance currents $\boldsymbol{i}_l = \begin{bmatrix} i_{ld} & i_{lq} \end{bmatrix}^{\mathrm{T}}$ as shown in (34).

$$\Delta\boldsymbol{A}_{ms}\boldsymbol{i}_m + \Delta\boldsymbol{B}_{ms}\boldsymbol{u}_i + \Delta\boldsymbol{C}_{ms}\boldsymbol{i}_e = \boldsymbol{C}_{msf}\boldsymbol{i}_l \tag{34}$$

The dynamic equation with modeling errors can be rewritten as (35) by substituting (34) into (33).

$$\dot{\boldsymbol{i}}_m = \boldsymbol{A}_{msf}\boldsymbol{i}_m + \boldsymbol{B}_{msf}\boldsymbol{u}_i + \boldsymbol{C}_{msf}\boldsymbol{i}_e + \boldsymbol{C}_{msf}\boldsymbol{i}_l \tag{35}$$

Based on the relationship between the disturbance currents $\boldsymbol{i}_l$ and the measurable currents $\boldsymbol{i}_m$ established in (35), the UICO is then designed as

$$\begin{aligned} \begin{bmatrix} \dot{\tilde{\boldsymbol{i}}}_m \\ \dot{\tilde{\boldsymbol{i}}}_l \end{bmatrix} = {} & \begin{bmatrix} \boldsymbol{A}_{msf} & \boldsymbol{C}_{msf} \\ \boldsymbol{0} & \boldsymbol{0} \end{bmatrix} \begin{bmatrix} \tilde{\boldsymbol{i}}_m \\ \tilde{\boldsymbol{i}}_l \end{bmatrix} + \begin{bmatrix} \boldsymbol{B}_{msf} & \boldsymbol{C}_{msf} \\ \boldsymbol{0} & \boldsymbol{0} \end{bmatrix} \begin{bmatrix} \boldsymbol{u}_i \\ \boldsymbol{i}_e \end{bmatrix} \\ & + \begin{bmatrix} \boldsymbol{H}_{c1} \\ \boldsymbol{H}_{c2} \end{bmatrix} \left(\boldsymbol{i}_m - \begin{bmatrix} \boldsymbol{I} & \boldsymbol{0} \end{bmatrix} \begin{bmatrix} \tilde{\boldsymbol{i}}_m \\ \tilde{\boldsymbol{i}}_l \end{bmatrix} \right) \end{aligned} \tag{36}$$

where $\tilde{\boldsymbol{i}}_m$ and $\tilde{\boldsymbol{i}}_l$ denote the estimated variables, and the UICO gain $\boldsymbol{H}_c = \begin{bmatrix} \boldsymbol{H}_{c1} & \boldsymbol{H}_{c2} \end{bmatrix}^{\mathrm{T}}$ is to drive the estimated variables to converge to the actual values. According to (36), the block diagram of the UICO is displayed in Fig. 10(a).

In a similar way, the UIVO can be designed to compensate for disturbance voltages $\boldsymbol{u}_l = \begin{bmatrix} u_{ld} & u_{lq} \end{bmatrix}^{\mathrm{T}}$. Referring to (35), the dynamic equation with disturbance voltages can be derived as

$$\dot{\boldsymbol{i}}_e = \boldsymbol{A}_{esf}\boldsymbol{i}_e + \boldsymbol{B}_{esf}\boldsymbol{u}_o + \boldsymbol{C}_{esf}\boldsymbol{i}_m + \boldsymbol{B}_{esf}\boldsymbol{u}_l. \tag{37}$$

The UIVO can then be designed based on the relationship between the disturbance voltages $\boldsymbol{u}_l$ and the measurable currents $\boldsymbol{i}_e$ as

$$\begin{aligned} \begin{bmatrix} \dot{\tilde{\boldsymbol{i}}}_e \\ \dot{\tilde{\boldsymbol{u}}}_l \end{bmatrix} = {} & \begin{bmatrix} \boldsymbol{A}_{esf} & \boldsymbol{B}_{esf} \\ \boldsymbol{0} & \boldsymbol{0} \end{bmatrix} \begin{bmatrix} \tilde{\boldsymbol{i}}_e \\ \tilde{\boldsymbol{u}}_l \end{bmatrix} + \begin{bmatrix} \boldsymbol{B}_{esf} & \boldsymbol{C}_{esf} \\ \boldsymbol{0} & \boldsymbol{0} \end{bmatrix} \begin{bmatrix} \boldsymbol{u}_e \\ \boldsymbol{i}_m \end{bmatrix} \\ & + \begin{bmatrix} \boldsymbol{H}_{v1} \\ \boldsymbol{H}_{v2} \end{bmatrix} \left(\boldsymbol{i}_e - \begin{bmatrix} \boldsymbol{I} & \boldsymbol{0} \end{bmatrix} \begin{bmatrix} \tilde{\boldsymbol{i}}_e \\ \tilde{\boldsymbol{u}}_l \end{bmatrix} \right) \end{aligned} \tag{38}$$

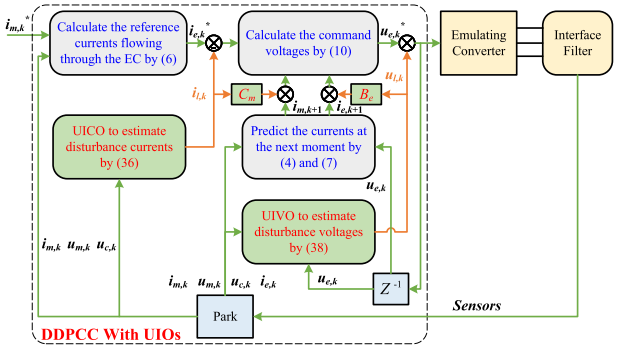

FIGURE 11. Block diagram of the DDPCC with disturbance observers.

and the block diagram of the UIVO is shown in Fig. 10(b). It should be noted that the UIVO gain $\boldsymbol{H}_v = \begin{bmatrix} \boldsymbol{H}_{v1} & \boldsymbol{H}_{v2} \end{bmatrix}^{\mathrm{T}}$ can be calculated by appropriate pole configuration according to the desired EME bandwidth, as well as the UICO gain $\boldsymbol{H}_c$. For instance, when the bandwidth of the EME is targeted at 500 Hz, the poles of both observers can be configured as $[-500\ -500\ -520\ -520]$ Hz, and the UICO and UIVO gains can thus be derived at each operating speed.

The observed disturbance currents and voltages can then be used to compensate for the prediction and control errors caused by model uncertainty. Since the system described by (2) and (3) is updated to the one defined by (35) and (37), new prediction, reference and output equations can be obtained based on the same processing steps in Section II-B. Comparing these new equations with (4), (6), (7), and (10), we can get the compensated system variables as

$$\begin{aligned} \boldsymbol{i}_{m,k+1}{}' &= \boldsymbol{i}_{m,k+1} + \boldsymbol{C}_m\tilde{\boldsymbol{i}}_{l,k} \\ \boldsymbol{i}_{e,k+1}{}' &= \boldsymbol{i}_{e,k+1} + \boldsymbol{B}_e\tilde{\boldsymbol{u}}_{l,k} \\ \boldsymbol{i}^*_{e,k}{}' &= \boldsymbol{i}^*_{e,k} - \tilde{\boldsymbol{i}}_{l,k} \\ \boldsymbol{u}^*_{e,k}{}' &= \boldsymbol{u}^*_{e,k} + \tilde{\boldsymbol{u}}_{l,k} \end{aligned} \tag{39}$$

and the block diagram of the DDPCC with disturbance suppression is shown in Fig. 11.

E. PARAMETER DESIGN FOR LCL FILTER

As mentioned above, the IF has a direct effect on system bandwidth and harmonic suppression. Moreover, inappropriate filter parameters can lead to system instability according to (24). However, to our knowledge, no universal method has been presented for sizing the parameters of the LCL filter in EMEs. In this section, each component of the LCL filter is designed based on theoretical analysis.

1) FILTER INDUCTANCE

As shown in Fig. 2, the actual currents are driven to track the references by controlling the terminal voltages of the EC. Thus, the actual currents involve the higher-order harmonics caused by switching frequency and lower-order harmonics introduced by dead time. A large inductance, although effective for harmonic suppression, narrows the system bandwidth. Here, the total inductance, $L_{total} = L_m + L_e$, is first derived

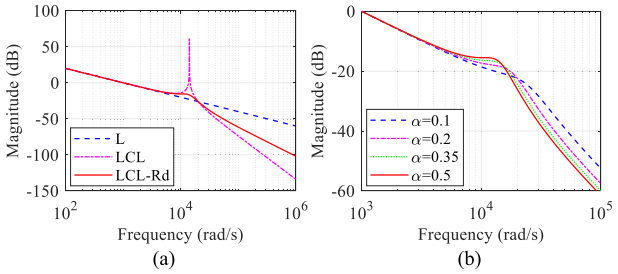

FIGURE 12. Bode diagrams of the IF. (a) Comparison of L, LC and LCL filters. (b) Comparison of the LCL filter with different inductance ratios.

from the suppression of lower-order harmonics, while the inductance ratio, $\alpha = L_m/L_{total}$, is determined by the suppression of higher-order harmonics.

According to (1), when the internal resistances of the inductors are neglected, the transfer function from u_e to i_m can be expressed as

$$G_f(s) = \frac{1}{(L_m + L_e)s} \frac{R_d C s + 1}{\frac{L_m L_e C}{L_m + L_e} s^2 + R_d C s + 1}. \tag{40}$$

In the low-frequency region, the transfer function can be simplified to (41). In this case, the LCL filter is equivalent to a first-order system, which is also shown in Fig. 12(a).

$$G_f(s) = \frac{1}{(L_m + L_e)s}. \tag{41}$$

In addition, as shown in Fig. 12(a), the LCL filter is more efficient at suppressing higher-order harmonics than the L filter for the same total inductance. Assuming that the lower-order harmonics introduced by the EC are the same as the MDU, the total inductance of the IF should be twice that of the actual machine to reach a close match, namely

$$L_{total} = L_m + L_e = 2L_s \tag{42}$$

where

$$L_s = \frac{L_d + L_q}{2}. \tag{43}$$

In practice, the switching frequency of the EC is usually much higher than that of the drive inverter to achieve better dynamic performance and emulating accuracy, which means less dead time and fewer low-order harmonics. Considering the system bandwidth and harmonic suppression, the total resistance can be designed as

$$L_{total} = (1.5 \sim 2)L_s \tag{44}$$

Once the total inductance is determined, the suppression of higher-order harmonics depends on the inductance ratio. Based on (40), the bode diagrams of the LCL filter with different inductance ratios are shown Fig. 12(b), in which only the ratios in the range of [0 0.5] are considered due to the same results for α and 1-α. As shown in Fig. 12(b), the filter has the strongest suppression of high-frequency harmonics at $\alpha = 0.5$, namely $L_m = L_e$. It should be noted that although the resonance peak is slightly higher for $\alpha = 0.5$, it can be conquered by selecting the resonant frequency reasonably.

TABLE 2. Parameters of the prototype PMSM and EME test benches.

Variable	Symbol	Value
PMSM Rated Power	P_r	2.6 kW
Load Motor Rated Power	P_{lr}	8 kW
PMSM Rated Speed	n_r	2500 r/min
PMSM Rated Torque	T_r	10 N·m
Stator Inductance (d-axis)	L_d	1.2 mH
Stator Inductance (q-axis)	L_q	1.2 mH
Stator Resistance	R_s	360 mΩ
Number of Pole Pairs	N_p	4
Filter Inductances	L_m, L_e	1 mH
Resistances of Filter Inductances	R_m, R_e	200 mΩ
Filter Capacitance	C	33 μF
Damping Resistance	R_d	30 Ω
Switching Frequency of MDU	f_{sw_m}	10 kHz
Switching Frequency of EME	f_{sw_e}	50 kHz
DC Link Voltage of MDU	V_{dc_m}	200 V
DC Link Voltage of EME	V_{dc_e}	300 V

2) FILTER CAPACITANCE

The resonant frequency of the LCL filter can be expressed as

$$\omega_{res} = \sqrt{\frac{L_m + L_e}{L_m L_e C}} \tag{45}$$

Obviously, after the filter inductances are determined, the resonant frequency depends on the capacitance. As shown in Fig. 12, the resonant frequency should be positioned away the operating frequency region of the actual machine to avoid a significant increase in current harmonics. Besides, the resonance position should ensure that the harmonics at the switching frequency can be effectively attenuated. Thus, the resonant frequency can be selected as

$$5\omega_{\max} < \omega_{res} < \omega_{pwm}/2 \tag{46}$$

The capacitance can subsequently be derived as

$$C = \frac{L_m + L_e}{L_m L_e {\omega_{res}}^2}. \tag{47}$$

3) DAMPING RESISTANCE

As shown in Fig. 12(a), the resonance peak of the LCL filter can be considerably attenuated by the damping resistor in series with the capacitor, thus reducing the harmonics at the resonant frequency and improving system stability. Also, a larger damping resistance appears to be more efficient in this case, whereas it may lead to instability according to (24). Considering the system stability and harmonic suppression at the resonant frequency, the damping resistance can be designed as

$$R_d = (0.5 \sim 0.7)\frac{L_m}{T_s} \tag{48}$$

Based on the previous analysis, the parameters of the LCL filter in this paper are designed as shown in Table 2.

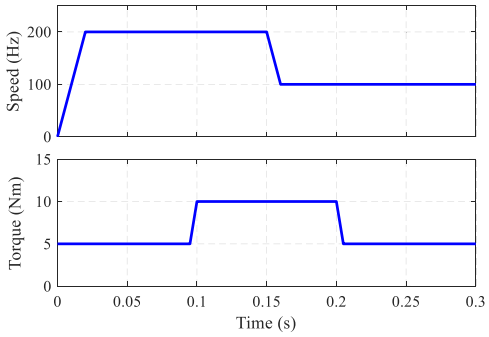

FIGURE 13. Transient speed and torque load profile for simulations.

III. SIMULATION RESULTS

The proposed EME based on LCL filter and DDPCC is first verified by simulations. The simulation topology is consistent with Fig. 2, where the drive inverter is operated with field-oriented control (FOC) in torque control command. The parameters of the EME test bench (i.e., the EME along with MDU under test) and target PMSM are shown in Table 2. To verify the steady-state and dynamic performance of the proposed EME over a wide operating point, a transient speed and torque load profile is designed as shown in Fig. 13, in which the motor is accelerated to 3000 r/min (i.e., $\omega_e = 200$ Hz) at start-up and stepped back to 1500 r/min (i.e., $\omega_e = 100$ Hz) at 0.15 s. Meanwhile, the torque steps from 5 N·m to 10 N·m at 0.1 s and steps back to 5 N·m at 0.2 s.

For comparison, the L filter-based EMEs with PI control [5] and OLCC [20] are also simulated respectively, and the results are shown in Fig. 14, in which the reference currents are calculated by the PMSM model. As shown in Fig. 14(a), the tracking errors of the L filter-based EME with PI control are as high as nearly 4 A and 0.8 A at machine start-up and high speed, respectively, which are much higher than those (0.76 A and 0.3 A) of the proposed EME. This is due to the distortion of high-frequency dynamic performance caused by the LPF effect of PI control. Besides, the tracking errors of the proposed EME are restricted to less than 0.2 A at low speed, which are still lower owing to the aforementioned control conflicts of the L filter-based EME.

As shown in Fig. 14(b), the tracking errors of the L filter-based EME with OLCC are apparently lower than that with PI control at machine start-up, since the OLCC can avoid control conflicts and greatly improve dynamic performance. However, the actual currents deviate significantly from the reference currents at both high and low speeds because the open-loop control cannot take into account the nonlinearities of the inverter, such as dead time and voltage drop. In fact, the tracking errors in this case are compensated by closed-loop current control of the MDU, so the actual currents can still match those of the target PMSM. Nevertheless, increased control requirements may result in the performance of the MDU not being convincingly verified. As shown in Fig. 14(c), both the steady-state and dynamic performance of the proposed EME are far superior to the other two cases, indicating that the proposed EME can reach a more accurate and reliable emulation. Furthermore, the target PMSM drive system where the actual motor rather than the EME is driven by the MDU is simulated and the currents are compared with the ones of the EME, as shown in Fig. 15. Not surprisingly, compared with the other two cases, the dq-axis current errors of the proposed EME are reduced by roughly half in most moments, which clearly gives stronger evidence that the proposed EME can achieve best emulating accuracy.

The comparison of the DDPCC with and without UIOs under parameter mismatch ($R_d = 1.6R_{d,real}$ and $L_m = L_e = 0.6L_{m,real} = 0.6L_{e,real}$) is carried out to verify the robustness. The reference disturbance currents and voltages are calculated by (49) and (50) presented in Appendix, respectively. As shown in Fig. 16, the d- and q-axis currents of the EME without UIOs certainly deviate from the references, while the disturbance currents and voltages can be exactly estimated by UIOs and compensated for modeling errors to maintain an accurate emulation. As expected, it can be found that the tracking errors caused by parameter mismatch is much larger at high speed. For this phenomenon, according to (49) and (50), the cross-coupling effect between d-axis and q-axis is enhanced at high speed, which amplifies the model errors caused by the inductance mismatch. Also, due to the high-frequency filtering effect of the capacitor branch, the current $i_{mq} - i_{eq}$ flowing through this branch increases at high speed, resulting in a remarkable increase in tracking errors caused by the resistance mismatch. Therefore, the disturbance compensation is necessary for the emulation of high-speed motors. Moreover, since the mismatches of L_m and L_e are set to be the same in this case and the forms of the UICO and UIVO are similar, the curve shapes of the disturbance currents and voltages are semblable accordingly, as shown in Fig. 16(c). To further verify the performance of the proposed UIOs, the dq-axis currents and estimated voltages and currents for the EME with UIOs under resistance mismatch and inductance mismatch are shown in Figs. 17 and 18, respectively. In these two cases, the dq-axis currents can still be evidently kept around the references, and disturbance voltages and currents are effectively evaluated. Also, it can be found that the higher-order harmonics of the disturbance voltages and currents is not able to be estimated due to the limitation of the system bandwidth, but it is sufficient to ensure an acceptable system stability and accuracy.

IV. EXPERIMENTAL RESULTS

The performance of the proposed EME is further verified by the experimental setup shown in Fig. 19(a). The drive inverter of the MDU is built by IGBT modules and controlled by a digital signal processor (DSP) TMS320F28335, while the EC is composed of Silicon Carbide (SiC) modules to reach a higher switching frequency. Typhoon HIL 602+ device is chosen as the RTS, where the lookup tables-based PMSM model is implemented on FPGA with a time step of 1 μs, while the proposed ICA is realized on ARM Cortex A9 with a time step of 20 μs. The parameters of the target PMSM and

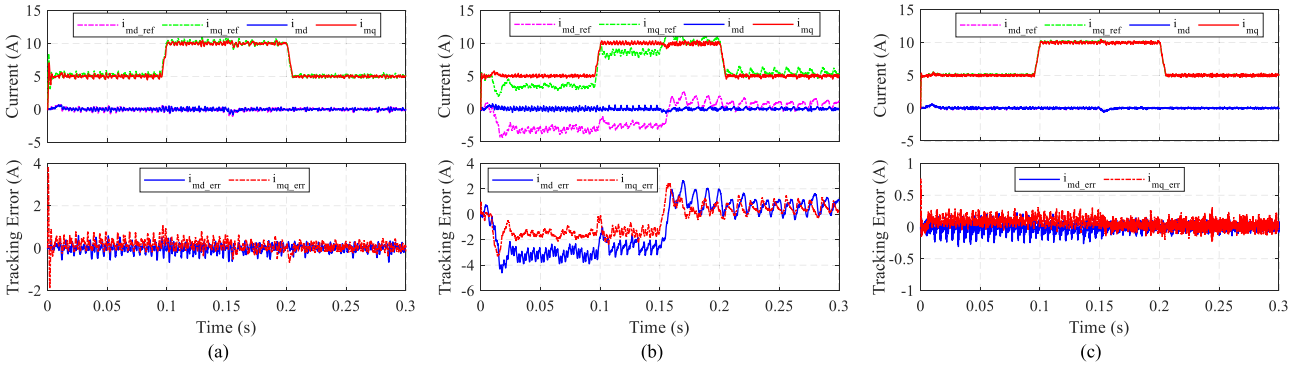

FIGURE 14. Simulation results of the current response of the EME with different IFs and ICAs. (a) L filter and PI control. (b) L filter and OLCC. (c) LCL filter and DDPCC.

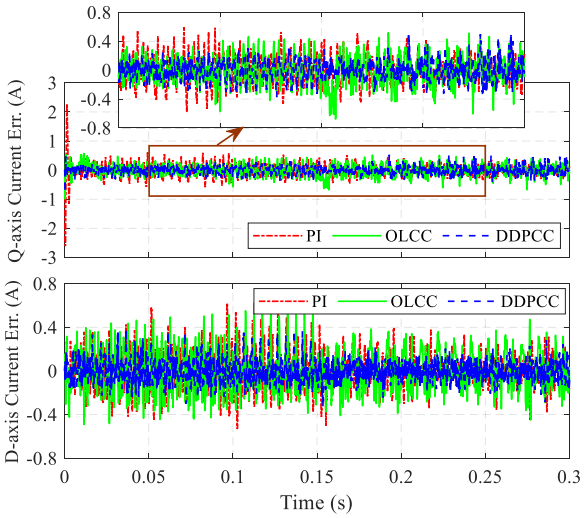

FIGURE 15. Simulation results of the current tracking error between the PMSM and EME with different IFs and ICAs.

EME test benches are listed in Table 2. The experiments are conducted under several transient conditions such as machine start-up, torque step change, and speed reversal. The results of the target PMSM test bench shown in Fig. 19(b) and the EME with the same topology but with *abc* frame-based model predictive control (MPC) [23] are also obtained for comparison. To fully validate the proposed EME, the FOC with speed control command is applied to the MDU.

The performance of the proposed EME without parameter mismatch is first verified. The current and speed responses of the actual PMSM, the EME with *abc* frame-based MPC, and the proposed EME under machine start-up are shown in Fig. 20. The operating speed is first set at 50 r/min, and then accelerated to 1200 r/min (i.e., $\omega_e = 80$ Hz) in 2 s. Meanwhile, the load torque is kept at 2 N·m. As can be seen, both the EMEs based on MPC and DDPCC can exactly emulate the fundamental current characteristics of the actual PMSM, and the corresponding speed errors can be controlled below 1% when the speed is greater than 400 r/min. However, the harmonic contents in the current of the EME based on MPC are much larger at low speed and low load, which leads to substantially increased higher-order current error (up to 1.8 A) and speed tracking errors (up to 6 r/min). This is partly due to the fact that the MPC based on *abc* frame is sensitive to phase current noise, which is sharply amplified for small currents. On the other hand, the time delay present in the system inevitably deteriorates the robustness. Whereas, the *dq* frame-based DDPCC with delay compensation thoroughly conquers these defects, thus achieving a more accurate emulation with reduced current error (less than 1 A) and speed error (less than 3 r/min).

The comparison of the current responses under torque step increase is presented in Fig. 21 to further verify the transient and steady-state performance, where the load torque steps from 1 N·m to 6 N·m in 20 ms and the operating speed is kept at 2500 r/min (i.e., $\omega_e = 166.7$ Hz). As expected, the proposed EME can maintain a reliable and satisfactory emulation of the target motor at a higher operating speed, and the errors of phase currents are bound to less than 0.5 A in both transient and steady state. Furthermore, the phase currents of the MPC-based EME are clearly distorted relative to the target motor at both low and high loads. Actually, as the sampling time is constant, the increased speed leads to larger prediction errors in phase currents for *abc* frame-based MPC. As a result, the emulated currents exhibit pronounced time-varying ac errors, which is particularly noticeable at high load, as shown in Fig. 21(d). In contrast, the much lower current errors and more matched waveforms of the proposed EME provide a direct proof for its high bandwidth and high precision. Fig. 22 shows the transient current responses under torque step drop to further verify the dynamic performance of the proposed EME, where the load torque steps from 8 N·m to 4 N·m in 10 ms and the operating speed is kept at 2000 r/min (i.e., $\omega_e = 133.3$ Hz). Evidently, the current error of the proposed EME can be effectively limited to below 1 A throughout the entire transient process, which is halved compared to that (up to 2.1 A) of the MPC-based EME. Hence, the degraded waveform quality and increased emulating error explicitly confirm the previous analysis.

Moreover, the speed reversal experiment is carried out, and the results are shown in Fig. 23, in which the load torque is kept at 5 N·m and the operating speed is reversed from 600 r/min to −600 r/min (i.e., ω_e from 40 Hz to −40 Hz)

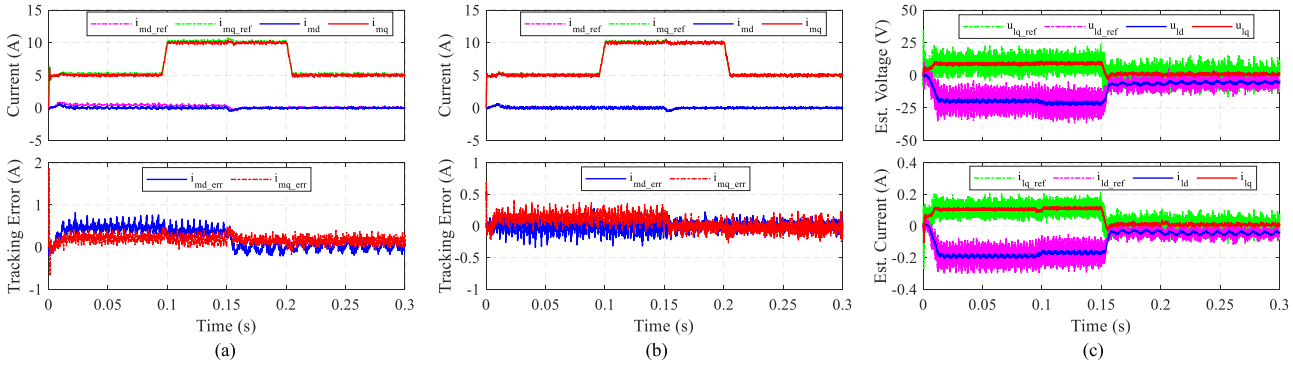

FIGURE 16. Simulation results of the comparison under $R_d = 1.6R_d^{real}$ and $L_m = L_e = 0.6L_m^{real} = 0.6L_e^{real}$. (a) Current response without UIOs. (b) Current response with UIOs. (c) Estimated disturbance voltages and currents of the UIOs.

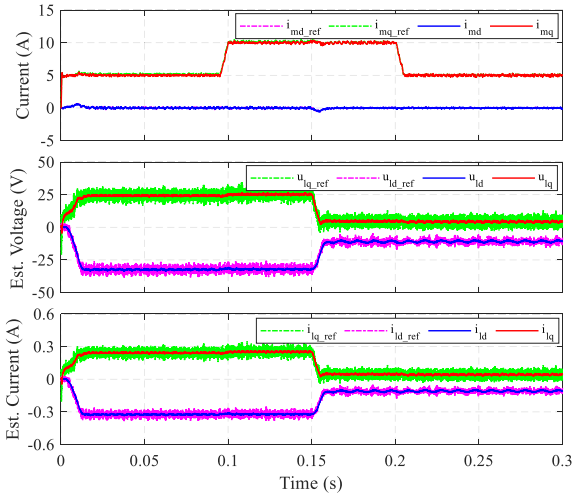

FIGURE 17. Simulation results of current response and estimated disturbance voltages and currents for the EME with UIOs under $R_d = 2R_d^{real}$.

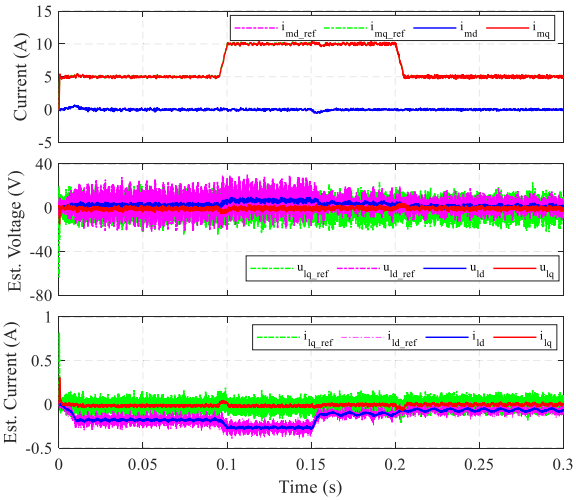

FIGURE 18. Simulation results of current response and estimated disturbance voltages and currents for the EME with UIOs under $L_m = L_e = 2L_m^{real} = 2L_e^{real}$.

in 2 s. In this case, although the steady-state performance of the MPC-based EME is improved owing to the reduction in the proportion of noise as the current amplitude increases, the

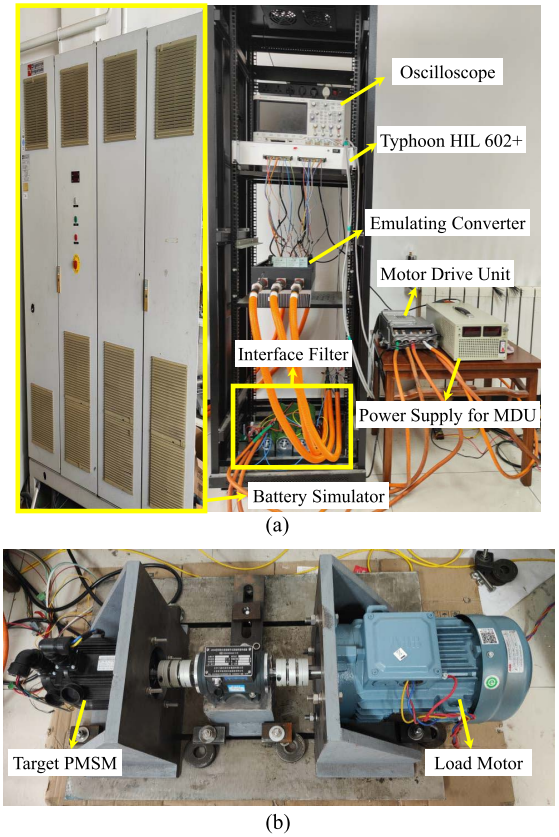

FIGURE 19. Experimental setups of (a) the proposed EME test bench and (b) target PMSM test bench.

significant current errors (up to 2.4 A) are produced during motor commutation due to the sharp changes in the amplitude and phase of the phase current, which results in an increased speed error (up to 6 r/min). Conversely, the current and speed responses of the proposed EME still closely match those of the actual PMSM, and its maximum speed error is below 4 r/min in transient state and less than 0.5% in steady state, proving that the proposed EME can reach an accurate emulation over a wide operating point.

The robustness of the proposed EME is then verified under parameter mismatch. The results of resistance mismatch, inductance mismatch, and both resistance and inductance

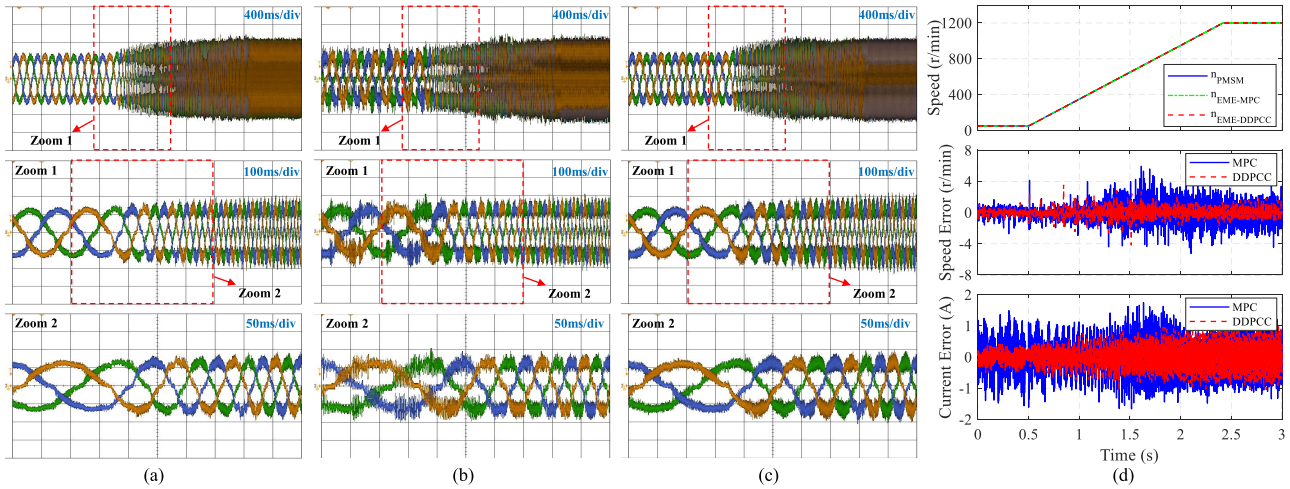

FIGURE 20. Experimental results of the current and speed responses under machine start-up. (a) Current response of the actual PMSM (Scale: 2 A/div). (b) Current response of the EME with *abc* frame-based MPC (Scale: 2 A/div). (c) Current response of the proposed EME with DDPCC (Scale: 2 A/div). (d) Comparison of the speed responses, speed errors and phase current errors.

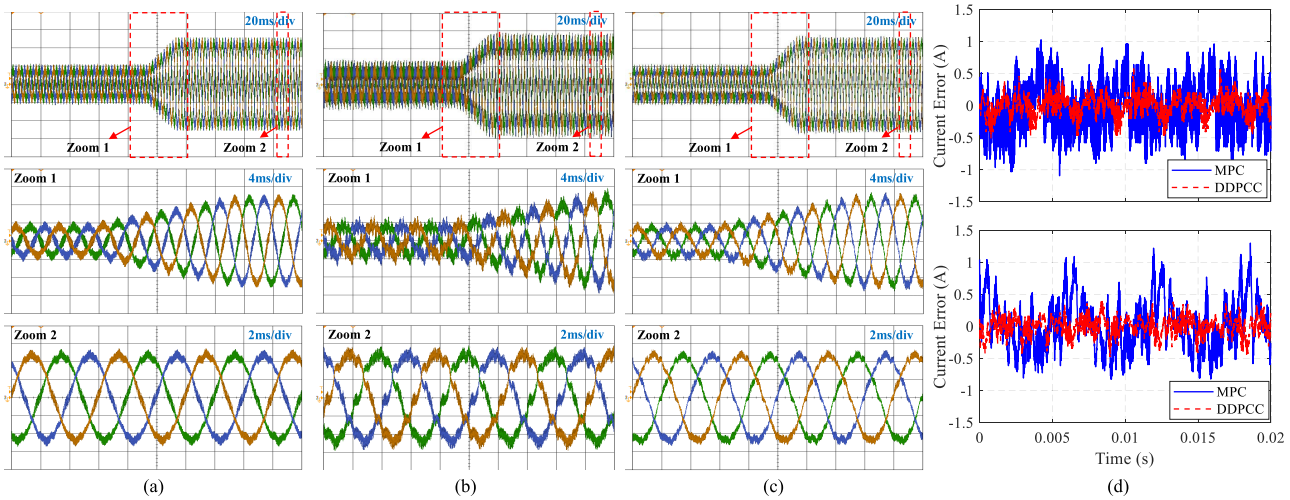

FIGURE 21. Experimental results of the current response under torque step increase at 2500 r/min. (a) The actual PMSM (Scale: 5 A/div). (b) The EME with *abc* frame-based MPC (Scale: 5 A/div). (c) The proposed EME with DDPCC (Scale: 5 A/div). (d) Comparison of the tracking errors in the phase current when load torque is 1 N·m (Top) and 6 N·m (Bottom).

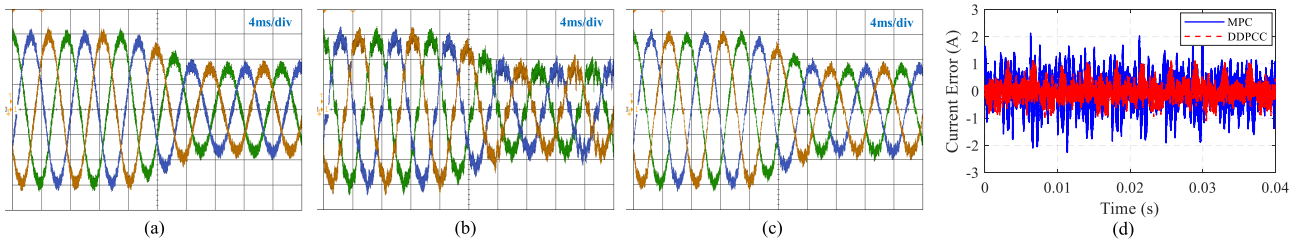

FIGURE 22. Experimental results of the current response under torque step drop at 2000 r/min. (a) The actual PMSM (Scale: 5 A/div). (b) The EME with *abc* frame-based MPC (Scale: 5 A/div). (c) The proposed EME with DDPCC (Scale: 5 A/div). (d) Comparison of the tracking errors in the phase current during the transient process.

mismatch are shown in Figs. 24, 25, and 26, respectively. The load torque steps from 3 N·m to 8 N·m at 0.3 s and the operating speed decreases from 1000 r/min to 600 r/min in 0.5 s at 0.8 s. Also, the tracking errors of the dq-axis currents in these cases at 1000 r/min and the load torque of 8 N·m is presented in Fig. 27. Under resistance mismatch, compared with the EME without UIOs, the maximum current error of the EME with UIOs is reduced from 1.6 A to 0.5 A as shown in Fig. 26(a) and (b), preliminary verifying the feasibility of disturbance compensation. Meanwhile, as shown in Fig. 24, the tracking errors of the EME without UIOs at high speed are much larger, which is because the increased current $i_{mq} - i_{eq}$ promotes the modeling errors caused by the resistance mismatch according to (49) and (50).

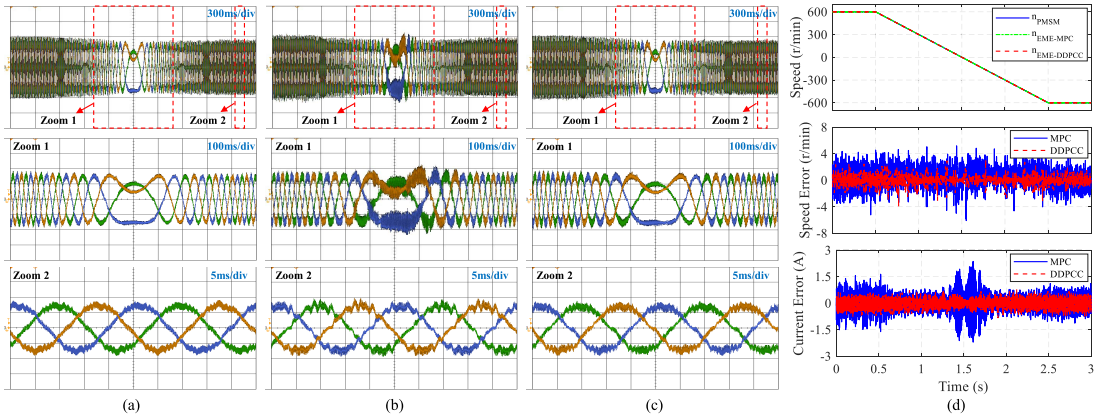

FIGURE 23. Experimental results of the current and speed responses under speed reversal change. (a) Current response of the actual PMSM (Scale: 4 A/div). (b) Current response of the EME with *abc* frame-based MPC (Scale: 4 A/div). (c) Current response of the proposed EME with DDPCC (Scale: 4 A/div). (d) Comparison of the speed responses, speed errors and phase current errors.

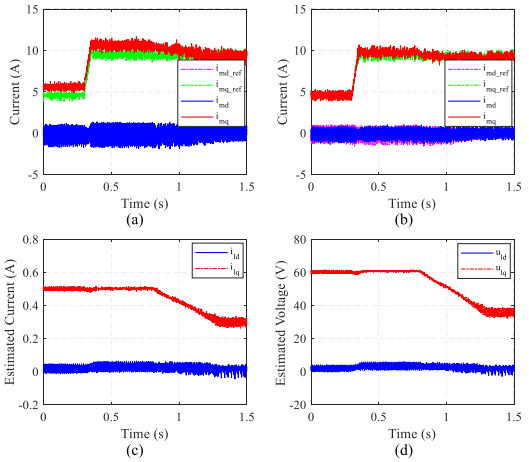

FIGURE 24. Experimental results of the comparison under $R_d = 2R_d^{real}$. Current response (a) without and (b) with UIOs. (c) Estimated disturbance currents of the UICO. (d) Estimated disturbance voltages of the UIVO.

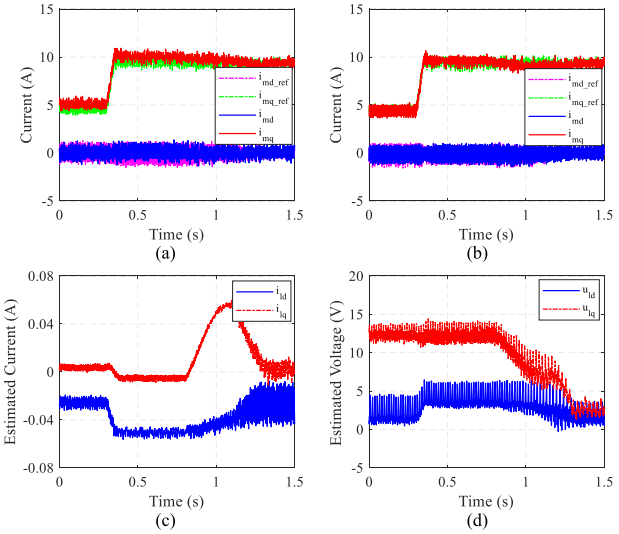

FIGURE 25. Experimental results of the comparison under $L_m = 2L_m^{real}$ and $L_e = 2L_e^{real}$. Current response (a) without and (b) with UIOs. (c) Estimated disturbance currents of the UICO. (d) Estimated disturbance voltages of the UIVO.

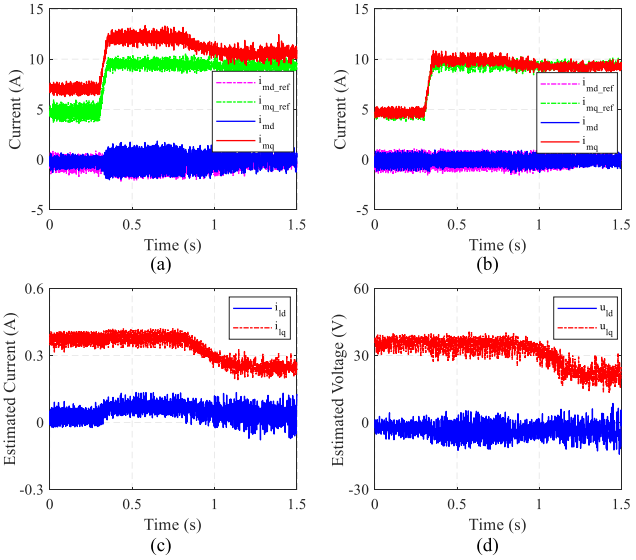

FIGURE 26. Experimental results of the comparison under $R_d = 1.6R_d^{real}$ and $L_m = L_e = 0.6L_m^{real} = 0.6L_e^{real}$. Current response (a) without and (b) with UIOs. (c) Estimated disturbance currents of the UICO. (d) Estimated disturbance voltages of the UIVO.

As can be seen from Fig. 25, disturbance currents and voltages under inductance mismatch are not only affected by the load torque but also by the operating speed, which is determined by the terms $\omega_e \boldsymbol{i}_m$ and $\omega_e \boldsymbol{i}_e$. In this case, the presence of UIOs is still able to lower the maximum tracking error from 1.3 A to 0.4 A. Further, since the disturbances generated by resistance mismatch and inductance mismatch are coupled to each other according to (49) and (50), it can be found that the addition of the inductance mismatch results in an evidently increased q-axis current deviation even with a smaller resistance mismatch by comparing Fig. 26 with Fig. 24. Again, the UIOs contributes to a remarkable reduction in tracking errors by approximately 78% (i.e., from 3.2 A to 0.7 A), which strongly proves the effectiveness of the UIOs.

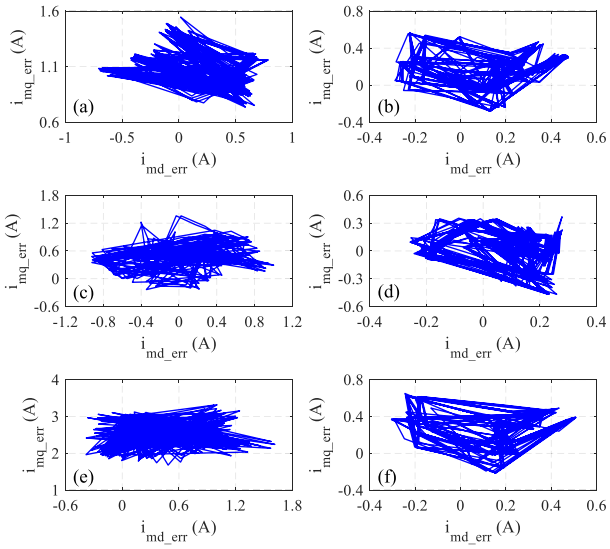

FIGURE 27. Experimental results of the tracking errors in dq-axis currents at 1000 r/min and 8 N·m. (a) Without and (b) with UIOs under $R_d = 2R_d^{real}$. (c) Without and (d) with UIOs under $L_m = L_e = 2L_m^{real} = 2L_e^{real}$. (e) Without and (f) with UIOs under $R_d = 1.6R_d^{real}$ and $L_m = L_e = 0.6L_m^{real} = 0.6L_e^{real}$.

V. CONCLUSION

In this paper, an EME based on LCL filter is presented to validate the performance of the MDU. A high-bandwidth DDPCC is proposed as the ICA in *dq* frame, which avoids control conflicts and greatly improves dynamic performance. The system stability and robustness are then analyzed in detail, and the UICO and UIVO are designed to suppress the disturbance currents and voltages caused by modeling errors. Furthermore, a theoretical method is presented for filter design, in which the harmonic suppression, bandwidth, stability, and resonance are all considered to reach an accurate and stable operation. To validate the proposed EME, several transient operating conditions are dedicatedly designed, and both the torque control mode and the speed control mode are adopted by the MDU. The comparisons between the proposed EME and earlier studies are carried out systematically. Simulation and experimental results show that the proposed EME can achieve fast, accurate and reliable emulation for the actual machine over a wide operating point under steady-state, transient and parameter mismatch conditions.

APPENDIX

According to (2) and (35), the actual disturbance currents can be expressed as

$$\begin{cases} i_{ld}^{ref} = \dfrac{1}{R_d}\left[\begin{array}{c}\Delta R_m i_{md} + \Delta L_m \frac{di_{md}}{dt} - \omega_e \Delta L_m i_{mq} \\ -\Delta R_d (i_{md} - i_{ed})\end{array}\right] \\ i_{lq}^{ref} = \dfrac{1}{R_d}\left[\begin{array}{c}\Delta R_m i_{mq} + \Delta L_m \frac{di_{mq}}{dt} + \omega_e \Delta L_m i_{md} \\ -\Delta R_d (i_{mq} - i_{eq})\end{array}\right] \end{cases} \tag{49}$$

where $\Delta R_m = R_m^{real} - R_m$, $\Delta L_m = L_m^{real} - L_m$, and $\Delta R_d = R_d^{real} - R_d$.

Similarly, the actual disturbance voltages is derived as

$$\begin{cases} u_{ld}^{ref} = \Delta R_e i_{ed} + \Delta L_e \dfrac{di_{ed}}{dt} - \omega_e \Delta L_e i_{eq} \\ \qquad -\Delta R_d (i_{ed} - i_{md}) \\ u_{lq}^{ref} = \Delta R_e i_{eq} + \Delta L_e \dfrac{di_{eq}}{dt} + \omega_e \Delta L_e i_{ed} \\ \qquad -\Delta R_d (i_{eq} - i_{mq}) \end{cases} \tag{50}$$

where $\Delta R_e = R_e^{real} - R_e$ and $\Delta L_e = L_e^{real} - L_e$.

REFERENCES

[1] F. F. M. El-Sousy, G. A. A. Aziz, M. Amin, K. Gaber, and O. A. Mohammed, "A high-speed microturbine PMa-SynRG emulation using power hardware-in-the-loop for wind energy conversion systems," *IEEE Access*, vol. 8, pp. 194612–194622, 2020.
[2] K. Saito and H. Akagi, "A power hardware-in-the-loop (P-HIL) test bench using two modular multilevel DSCC converters for a synchronous motor drive," *IEEE Trans. Ind. Appl.*, vol. 54, no. 5, pp. 4563–4573, Sep. 2018.
[3] S. Jakubek, E. Luchini, A. Oberhummer, and F. Pfister, "A model-based interfacing concept for accurate power hardware-in-the-loop systems," *Math. Comput. Model. Dyn. Syst.*, vol. 22, no. 1, pp. 1–20, Jan. 2016.
[4] M.-Y. Wang and D.-F. Wang, "A desktop electric machine emulator implementation method based on phase voltage reconstruction," *IEEE Access*, vol. 8, pp. 97698–97706, 2020.
[5] K. S. Amitkumar, R. S. Kaarthik, and P. Pillay, "A versatile power-hardware-in-the-loop-based emulator for rapid testing of transportation electric drives," *IEEE Trans. Transport. Electrific.*, vol. 4, no. 4, pp. 901–911, Dec. 2018.
[6] J. Tian, J. Liu, J. Shu, J. Tang, and J. Yang, "Engineering modelling of wind turbine applied in real-time simulation with hardware-in-loop and optimising control," *IET Power Electron.*, vol. 11, no. 15, pp. 2490–2498, Nov. 2018.
[7] D. S. Junior, J. G. Oliveira, P. D. Almeida, and C. Bostrom, "Control of a multi-functional inverter in an AC microgrid—Real-time simulation with control hardware in the loop," *Electr. Power Syst. Res.*, vol. 172, pp. 201–212, Jul. 2019.
[8] M. A. Masadeh, K. S. Amitkumar, and P. Pillay, "Power electronic converter-based induction motor emulator including main and leakage flux saturation," *IEEE Trans. Transport. Electrific.*, vol. 4, no. 2, pp. 483–493, Jun. 2018.
[9] O. Vodyakho, M. Steurer, C. S. Edrington, and F. Fleming, "An induction machine emulator for high-power applications utilizing advanced simulation tools with graphical user interfaces," *IEEE Trans. Energy Convers.*, vol. 27, no. 1, pp. 160–172, Mar. 2012.
[10] A. Schmitt, J. Richter, M. Gommeringer, T. Wersal, and M. Braun, "A novel 100 kW power hardware-in-the-loop emulation test bench for permanent magnet synchronous machines with nonlinear magnetics," in *Proc. 8th IET Int. Conf. (PEMD)*, 2016, pp. 1–6.
[11] H. Cui, J. Xu, and M. Xing, "Power-hardware-in-the-loop simulator for brushless DC motor," in *Proc. 43rd Annual Conf. IEEE Ind. Electron. Soc. (IECON)*, Oct. 2017, pp. 2121–2126.
[12] X. Jiaqun, X. Meili, and Z. Hongqiang, "Universal power-hardware-in-the-loop simulator for BLDCM and PMSM," *J. Magn.*, vol. 24, no. 3, pp. 454–462, Sep. 2019.
[13] F. Xu, V. Dinavahi, and X. Xu, "Hybrid analytical model of switched reluctance machine for real-time hardware-in-the-loop simulation," *IET Electr. Power App.*, vol. 11, no. 6, pp. 1114–1123, Jul. 2017.
[14] G. Lauss and K. Strunz, "Accurate and stable hardware-in-the-loop (HIL) real-time simulation of integrated power electronics and power systems," *IEEE Trans. Power Electron.*, vol. 36, no. 9, pp. 10920–10932, Sep. 2021.
[15] Y. S. Rao and M. C. Chandorkar, "Real-time electrical load emulator using optimal feedback control technique," *IEEE Trans. Ind. Electron.*, vol. 57, no. 4, pp. 1217–1225, Apr. 2010.
[16] M. Ashourianjozdani, L. A. C. Lopes, and P. Pillay, "Power electronic converter based PMSG emulator: A testbed for renewable energy experiments," *IEEE Trans. Ind. Appl.*, vol. 54, no. 4, pp. 3626–3636, Jul. 2018.
[17] R. S. Kaarthik, K. S. Amitkumar, and P. Pillay, "Emulation of a permanent-magnet synchronous generator in real-time using power hardware-in-the-loop," *IEEE Trans. Transp. Electrific.*, vol. 4, no. 2, pp. 474–482, Jun. 2018.

[18] L. Zhu, D. Jiang, R. Qu, L. M. Tolbert, and Q. Li, "Design of power hardware-in-the-loop simulations for integrated starter–generator systems," *IEEE Trans. Transp. Electrific.*, vol. 5, no. 1, pp. 80–92, Mar. 2019.
[19] K. S. Amitkumar, R. Thike, and P. Pillay, "Linear amplifier-based power-hardware-in-the-loop emulation of a variable flux machine," *IEEE Trans. Ind. Appl.*, vol. 55, no. 5, pp. 4624–4632, Sep. 2019.
[20] Y. Qi, K. Ma, and W. Tang, "Full-bandwidth mission profile emulation of the electric machine system with voltage reference signal transmission," *IEEE Trans. Power Electron.*, vol. 37, no. 3, pp. 3473–3483, Mar. 2022.
[21] X. Zou, X. Xiao, P. He, and Y. Song, "Permanent magnet synchronous machine emulation based on power hardware-in-the-loop simulation," in *Proc. IEEE Int. Electr. Mach. Drives Conf. (IEMDC)*, May 2019, pp. 248–253.
[22] K. Ma and Y. Song, "Power-electronic-based electric machine emulator using direct impedance regulation," *IEEE Trans. Power Electron.*, vol. 35, no. 10, pp. 10673–10680, Oct. 2020.
[23] S. Lentijo, S. D'Arco, and A. Monti, "Comparing the dynamic performances of power hardware-in-the-loop interfaces," *IEEE Trans. Ind. Electron.*, vol. 57, no. 4, pp. 1195–1207, Apr. 2010.
[24] A. Monti, S. D'Arco, Y. Work, and A. Lentini, "A virtual testing facility for elevator and escalator systems," in *Proc. IEEE Power Electron. Specialists Conf.*, Jun. 2007, pp. 820–825.
[25] C. Poongothai and K. Vasudevan, "Design of *LCL* filter for grid-interfaced PV system based on cost minimization," *IEEE Trans. Ind. Appl.*, vol. 55, no. 1, pp. 584–592, Jan. 2019.
[26] Y. Kim and H. Kim, "Optimal design of LCL filter in grid-connected inverters," *IET Power Electron.*, vol. 12, no. 7, pp. 1774–1782, Jun. 2019.
[27] X. Chen, J. Wang, B. Sen, P. Lazari, and T. Sun, "A high-fidelity and computationally efficient model for interior permanent-magnet machines considering the magnetic saturation, spatial harmonics, and iron loss effect," *IEEE Trans. Ind. Electron.*, vol. 62, no. 7, pp. 4044–4055, Jul. 2015.
[28] J. Song, C. Fu, G. Zhang, B. Duan, and C. Zhang, "Backstepping control of high-frequency link matrix rectifier for battery chargers," *IEEE Trans. Power Electron.*, vol. 36, no. 9, pp. 10801–10814, Sep. 2021.
[29] T. Li, X. Liu, and H. Yu, "Backstepping nonsingular terminal sliding mode control for PMSM with finite-time disturbance observer," *IEEE Access*, vol. 9, pp. 135496–13507, 2021.
[30] L. Niu, M. Yang, G. Wang, and D. Xu, "Research on the robust current control algorithm of permanent magnet synchronous motor based on deadbeat control principle," in *Proc. CSEE*, vol. 33, no. 15, 2013, pp. 78–85.
[31] Y. Wang, Y. Feng, X. Zhang, and J. Liang, "A new reaching law for antidisturbance sliding-mode control of PMSM speed regulation system," *IEEE Trans. Power Electron.*, vol. 35, no. 4, pp. 4117–4126, Apr. 2020.
[32] X. Liu and H. Yu, "Continuous adaptive integral-type sliding mode control based on disturbance observer for PMSM drives," *Nonlinear Dyn.*, vol. 104, no. 2, pp. 1429–1441, Mar. 2021.
[33] T. Li and X. Liu, "Non-cascade fast nonsingular terminal sliding mode control of permanent magnet synchronous motor based on disturbance observers," *J. Electr. Eng. Technol.*, vol. 17, no. 2, pp. 1061–1075, Mar. 2022.
[34] X. Liu, H. Yu, J. Yu, and Y. Zhao, "A novel speed control method based on port-controlled Hamiltonian and disturbance observer for PMSM drives," *IEEE Access*, vol. 7, pp. 111115–111123, 2019.
[35] W. Chen, J. Yang, L. Guo, and S. Li, "Disturbance-observer-based control and related methods—An overview," *IEEE Trans. Ind. Electron.*, vol. 63, no. 2, pp. 1083–1095, Feb. 2016.
[36] A. Chakrabarty, R. Ayoub, S. H. Żak, and S. Sundaram, "Delayed unknown input observers for discrete-time linear systems with guaranteed performance," *Syst. Control Lett.*, vol. 103, pp. 9–15, May 2017.

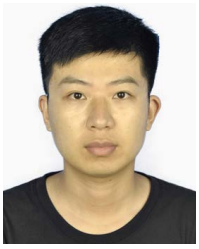

QINGLE SUN was born in Shandong, China, in 1995. He received the B.S. degree in vehicle engineering from the Taiyuan University of Technology, Shanxi, China, in 2018.

He is currently pursuing the Ph.D. degree with the National Engineering Research Center of Electric Vehicles, School of Mechanical Engineering, Beijing Institute of Technology. His research interests include electric machine emulator, multilevel converter, and power electronics.

ZHIFU WANG was born in Shandong, China, in 1977. He received the M.S. and Ph.D. degrees in vehicle engineering from the Beijing Institute of Technology, Beijing, China, in 2003 and 2013, respectively.

He is currently an Assistant Professor with the National Engineering Research Center of Electric Vehicles, School of Mechanical Engineering, Beijing Institute of Technology. His research interests include the motor control, vehicle dynamics, and electric machine emulator.

ZESHANG WANG received the B.S. degree in vehicle engineering from the Harbin Institute of Technology, Weihai, Shandong, China, in 2021. He is currently pursuing the M.S. degree with the National Engineering Research Center of Electric Vehicles, School of Mechanical Engineering, Beijing Institute of Technology.

His research interests include electric machine emulator and motor control.

WENMEI HAO was born in Hebei, China, in 1993. She received the B.Sc. and Ph.D. degrees in electrical engineering from Beijing Jiaotong University, China, in 2016 and 2022, respectively.

She was a Visiting Ph.D. Scholar at Politecnico di Torino, Italy, from December 2019 to February 2021. She is currently a Postdoctoral Researcher with the National Engineering Research Center of Electric Vehicles, School of Mechanical Engineering, Beijing Institute of Technology, China. Her current research interests include wireless charging technology and power electronics.